Small Molecule Inhibitors that Disrupt the MTDH-SND1 Complex Suppress Breast Cancer Progression and Metastasis

Minhong Shen[1], **Yong Wei**[1], **Hahn Kim**[2,3], **Liling Wan**[1], **Yi-Zhou Jiang**[4], **Xiang Hang**[1], **Michael Raba**[5], **Stacy Remiszewski**[6], **Michelle Rowicki**[1], **Cheng-Guo Wu**[7], **Songyang Wu**[4], **Lanjing Zhang**[8], **Xin Lu**[1], **Min Yuan**[1], **Heath A. Smith**[1], **Aiping Zheng**[7], **Joseph Bertino**[9,10], **John F. Jin**[11], **Yongna Xing**[7], **Zhi-Ming Shao**[4], **Yibin Kang**[1,12,13,*]

[1]Department of Molecular Biology, Princeton University, Princeton, NJ 08544, USA

[2]Department of Chemistry, Princeton University, Princeton, NJ 08544, USA

[3]Princeton University Small Molecule Screening Center, Princeton University, Princeton, NJ 08544, USA

[4]Department of Breast Surgery, Fudan University Shanghai Cancer Center; Department of Oncology, Shanghai Medical College, Fudan University, P.R. China

[5]Crelux GmgH, Martinsried, Germany

[6]SWR Pharma Consulting LLC, Princeton USA

[7]McArdle Laboratory for Cancer Research, Department of Oncology, University of Wisconsin-Madison, School of Medicine and Public Health, Madison, WI 53706, USA

[8]Department of Pathology, University Medical Center of Princeton, Plainsboro, New Jersey; and Rutgers Cancer Institute of New Jersey, New Brunswick, New Jersey

[9]Pharmacokinetics and Pharmacodynamics (PK/PD) Shared Resource, Rutgers Cancer Institute of New Jersey Rutgers, The State University of New Jersey, New Brunswick, NJ 08901, USA

*Correspondence: Yibin Kang, Ph.D., Department of Molecular Biology, Washington Road, LTL 255, Princeton University, Princeton, NJ 08544, Phone: (609) 258-8834; Fax: (609) 258-2340, ykang@princeton.edu.

[10]Robert Wood Johnson Medical School Rutgers, The State University of New Jersey, New Brunswick, NJ 08901, USA

[11]Firebrand Therapeutics, 174 Nassaue Street, #331, Princeton, NJ, 08542, USA

[12]Cancer Metabolism and Growth Program, Rutgers Cancer Institute of New Jersey, New Brunswick, NJ, 08903, USA

[13]Ludwig Institute for Cancer Research Princeton Branch, Princeton, USA

Abstract

Metastatic breast cancer is leading health burden worldwide. Previous studies have shown that Metadherin (MTDH) promotes breast cancer initiation, metastasis and therapy resistance; however, the therapeutic potential of targeting MTDH remains largely unexplored. Here, we used genetically modified mice and demonstrate that genetic ablation of *Mtdh* inhibits breast cancer development through disrupting the interaction with *Staphylococcal* nuclease domain-containing 1 (SND1) which is required to sustain breast cancer progression in established tumors. We performed a small molecule compound screening to identify a class of specific inhibitors that disrupt the protein-protein interaction between MTDH-SND1, and show that our lead candidate compounds C26-A2 and C26-A6 suppressed tumor growth and metastasis, and enhanced chemotherapy sensitivity in preclinical models of triple-negative breast cancer. Our results demonstrate a significant therapeutic potential in targeting the MTDH-SND1 complex and identify a new class of therapeutic agents for metastatic breast cancer.

Introduction

The lack of effective therapy for metastatic cancer and the frequent resistance to treatments are the two most significant hurdles for reducing the mortality of metastatic breast cancer[1]. We previously used computational analysis of gene expression profiles of breast tumor samples to identify *MTDH/AEG1* as a key driver gene in poor-prognosis breast cancers[2,3]. Functionally, MTDH is an important mediator of tumor initiation, chemoresistance and metastasis[2,4]. Global *Mtdh* knockout in mice does not affect embryogenesis or postnatal development, but profoundly impairs the formation of mammary tumors[4]. Similar results were obtained from whole body genetic knockout studies of MTDH/AEG1 in the context of prostate cancer, liver, lung and colorectal cancers[5–7]. These findings suggested that *Mtdh* is specifically required for malignant tumors but is dispensable for normal development or homeostasis, underscoring the rationale to therapeutically target MTDH in cancer. However, the biochemical and molecular mechanisms of MTDH in breast cancer remain poorly defined. To uncover the functional partners underlying MTDH's tumor promoting role in breast cancer, we performed MTDH immunoprecipitation followed by mass spectrum analysis, and identified *Staphylococcal* nuclease domain-containing 1 (SND1) as a major MTDH-interacting partner[8,9]. SND1 has been previously characterized as a transcriptional co-activator[10] or a RNA binding protein that is involved in the regulation of RNA stability, splicing, and editing[10,11]. Most importantly, SND1 shares similar clinical and functional importance as MTDH in promoting metastasis and chemoresistance[4,6,8]. Furthermore, the tumor-promoting function of MTDH is crucially dependent on the interaction with SND1[4].

We have previously resolved the crystal structure of MTDH-SND1 complex[12] and revealed a unique interface between the two N-terminal SN domains of SND1 and a peptide motif of MTDH. The surface contour of SND1 revealed two deep pockets that specifically interact with the MTDH residues. In particular, the bulky and hydrophobic side chains of W394 and W401 of MTDH were found to bind deeply into the two hydrophobic binding pockets of SND1[12]. Point mutations of these two evolutionarily conserved tryptophan residues in MTDH, which blocked the interaction with SND1, also completely eliminated the tumor-supportive function of MTDH[4,12]. Notably, the two binding pockets possess ideal structural, geometrical and biochemical properties suitable for the development of small molecule inhibitors[12].

In this study, we generated breast cancer mouse models with inducible *Mtdh* knockout to evaluate the requirement of the MTDH-SND1 complex in the late stage breast cancer progression and metastasis. We further developed a small molecule screening platform to discover compounds that block MTDH-SND1 interaction and evaluate their therapeutic efficacy.

Results

Mtdh acute KO inhibits metastatic breast cancer progression

To evaluate the therapeutic potential of targeting MTDH in established tumors, we generated *Mtdh* conditional knockout strain. Mouse ESC cells with two loxp sites flanking exon 3 of *Mtdh* were injected into C57BL/6N strain to derive the *Mtdh*$^{fl/fl}$ strain (Fig. 1a). The C57BL/6N.*Mtdh*$^{fl/fl}$ strain was then backcrossed to FVB for more than 10 generations to change the genetic background to FVB. Splenocytes from *FVB.Mtdh*$^{fl/fl}$ were isolated and infected with Cre-expressing adenovirus to validate Cre-mediated *Mtdh* knockout (KO) (Fig. 1a). Next, the *FVB.Mtdh*$^{fl/fl}$ strain was crossed with *FVB.UBC-Cre*$^{ERT+/-}$ to generate *FVB.UBC-Cre*$^{ERT+/-}$*;Mtdh*$^{fl/fl}$, in which *Mtdh* is depleted upon 5 days of i.p. Tamoxifen (Tmx) treatment at 60 mg/kg (Fig. 1b). Such a dosing regimen of tamoxifen was commonly used in conditional KO of gene of interest in mouse cancer models including MMTV-PyMT and has been shown to have no direct effect on PyMT tumor growth and metastasis[13,14]. Finally, *FVB.UBC-Cre*$^{ERT+/-}$*;Mtdh*$^{fl/fl}$ were crossed with the FVB.MMTV-PyMT strain, and the resulted female *PyMT; UBC-Cre*$^{ERT+/-}$*;Mtdh*$^{fl/fl}$ mice developed spontaneous mammary tumors with *Mtdh* inducible KO upon Tmx treatment (Fig. 1c).

Female *PyMT;UBC-Cre*$^{ERT+/-}$*;Mtdh*$^{fl/fl}$ mice were separated into two groups when primary tumors were established (Fig. 1c,d). The mice were randomized and matched by tumor size (Fig. 1d), followed by Tmx or vehicle treatments. Tmx induced *Mtdh* acute loss significantly suppresses primary tumor development, reduces spontaneous metastasis, and prolongs mouse survival (Fig. 1e–h, and Extended Data Fig. 1a,b). We also crossed *UBC-Cre*$^{ERT+/-}$*;Mtdh*$^{fl/fl}$ with *C3* and *MMTV-Wnt* mouse strains that develop breast tumors of basal subtype[15–17] or diverse subtypes[18–20], respectively. In both models, acute *Mtdh* loss also suppressed tumor growth and lung metastasis (Extended Data Fig. 1c–n). Furthermore, immunohistochemistry (IHC) staining indicated that *Mtdh* acute KO dramatically inhibits tumor proliferation and increases apoptosis (Extended Data Fig. 2a,b). Collectively, the

results indicated that *Mtdh* acute loss in established tumors suppresses breast cancer progression and metastasis, underlying the therapeutic potential of targeting MTDH.

MTDH-SND1 sustains tumor progression and metastasis

We previously found that MTDH-SND1 interaction is essential for sustaining tumor initiating cell activities during early tumorigenesis of PyMT, Wnt, Neu and carcinogen-induced mammary gland tumors and in *in vitro* tumorsphere formation analysis[4]. However, whether this interaction is still required for late stages of breast cancer progression is still unknown and is paramount for further clinical development of MTDH-targeting therapeutics in human patients. To address this question, we first generated a mammary tumor cell line derived from *PyMT;UBC-Cre^{ERT+/−};Mtdh^{fl/fl}* tumors. Similar to these tumors *in vivo*, *Mtdh* can be genetically deleted with 4-OHT treatment of this cell line in cell culture (Fig. 2a). 4-OHT treatment induced MTDH KO leading to a significant decrease in tumorsphere formation (Fig. 2b and Extended Data Fig. 2c,d). In contrast, 4-OHT treatment no longer affects the spheres that formed by *PyMT;UBC-Cre^{ERT+/−};Mtdh^{fl/fl}* cells pretreated with 4-OHT (Extended Data Fig. 2c,d), suggesting that the reduction in tumorsphere upon 4-OHT treatment is due to the acute *Mtdh* KO rather than any inhibitory effect of 4-OHT itself.

Next, *PyMT;UBC-Cre^{ERT+/−};Mtdh^{fl/fl}* tumor cells were injected into FVB female mice orthotopically, and after primary tumors were established (Fig. 2c), the mice were treated with or without Tmx. Consistent with the results shown above, *Mtdh* acute KO in allograft tumors dramatically inhibits primary tumor growth and spontaneous lung metastasis (Fig. 2d,e and Extended Data Fig. 2e–g).

Taking advantage of the *PyMT;UBC-Cre^{ERT+/−};Mtdh^{fl/fl}* cell line, we next generated rescue lines with stable lentiviral expression of wild type (MTDH-WT) or SND1 interaction-deficient MTDH-W391D (MTDH-13D) (Fig. 2f)[4,12]. Tumorsphere assays indicated that wild type MTDH, but not SND1 interaction deficient MTDH-13D mutant, was able to successfully rescue both tumorsphere number and size of the cell line upon acute MTDH-KO by 4-OHT treatment versus vehicle control (Fig. 2g). On the other hand, 4-OHT treatment of 4-OHT pretreated cells did not affect sphere formation, again confirming no inhibitory side effect from 4-OHT exposure *per se* (Extended Data Fig. 2h). Next, these cell lines were injected orthotopically into FVB females followed by Tmx or vehicle treatment after tumors had been established. Consistent with the *in vitro* assay, wild type MTDH but not MTDH-13D restores primary tumor growth and metastasis (Fig. 2h,i), validating the importance of MTDH-SND1 interaction in maintaining breast cancer progression and metastasis.

Discovery of small chemical inhibitors of MTDH-SND1

Given that MTDH-SND1 interaction is critical for breast cancer progression (Fig. 2 and Extended Data Fig. 2c–h) and the interaction is dependent on the two small pockets formed by SND1 that might be targeted by small chemical compounds[12], we set out to identify small chemical inhibitors that can disrupt MTDH-SND1 interaction by binding to these pockets. To this end, we established luciferase and FRET assays to screen a singleton small chemical library consisting of ~50,000 compounds with high structural diversity.

To generate a luciferase-based screening system, firefly luciferase was split into N- and C-terminals according to previous studies[21–23]. Both N- and C-terminal domains alone have almost undetectable luciferase activity (Extended Data Fig. 3a). Next, the two fragments were fused to SND1 and MTDH interaction domains respectively to generate SND1-NLuc and CLuc-MTDH (Split-luc) (Fig. 3a, left). Similarly, SND1-NLuc or CLuc-MTDH alone, or co-expression of SND1-NLuc and CLuc or CLuc-MTDH and NLuc did not produce significant luciferase signals either (Extended Data Fig. 3a). However, when SND1-NLuc+CLuc-MTDH were co-expressed, N- and C-terminal domains of the luciferase fragments were brought close to each other due to the interaction between SND1 and MTDH, and substantial luciferase activity was reconstituted (Fig. 3a, left and Extended Data Fig. 3a). The interaction between SND1-NLuc and CLuc-MTDH was also validated with co-immunoprecipitation (Co-IP) experiments (Extended Data Fig. 3b). In the presence of the compounds (inhibitors) that block MTDH-SND1 interaction, the reconstitution of luciferase activity is expected to be reduced (Fig. 3a, left). Meanwhile, considering the possibility that compounds capable of directly inhibiting the enzymatic activity of luciferase could also result in lower luciferase signal without any blocking effect on MTDH-SND1 interaction, we generated Linked-luc that directly fuse NLuc and CLuc together to be used in counter screening (Fig. 3a, right).

To further confirm the specificity of the system, wild type MTDH (MTDH-WT) (PNSDWNAPAEEWGNW) minimal peptide that binds to SND1 in the two hydrophobic pockets and its mutant (PNSD**A**NAPAEE**A**GNW) form (MTDH-MT) with the two key tryptophans mutated to alanines and lack SND1 binding ability[12] were synthesized. MTDH-WT peptide but not the mutant significantly inhibits split-luc activity (Extended Data Fig. 3c). On the other hand, linked-luc activity was not affected by either MTDH-WT or MTDH-MT peptides (Extended Data Fig. 3c). These results suggested that the split-luc assay can be used as a readout to identify inhibitors that block MTDH-SND1 interaction.

Next, a FRET assay was established for secondary screening by fusing MTDH interaction domain with CFP and labeling SND1 domain with TC-FLASH[24]. MTDH-SND1 interaction allows FRET signal to be detected, whereas the signal would be interrupted in the presence of MTDH-SND1 inhibitors (Fig. 3b). Similar to the split-luciferase assay, MTDH-WT and MTDH-MT peptides were employed to validate the specificity of the FRET assay in detecting the disruption of MTDH-SND1 interaction (Extended Data Fig. 3d).

Using the screening systems described above, a 50K singleton library was first screened with the spit-luc assay with a repeat (Supplementary Tables 1 and 2). Compounds that showed inhibitory efficiency of 0.4 or above in either one of the two rounds of screening were selected and repeated with split-luc, linked-luc and FRET assays (Supplementary Table 3). A set of criteria (see Methods section) was applied to narrow down the candidate list to 52 compounds (Supplementary Tables 4 and 5). Luciferase and FRET assays were performed again for these 52 candidates and the best 12 were picked for split-luc assay in various concentrations to calculate the IC50 (Fig. 3c and Supplementary Tables 5 and 6). Using these criteria, we finally focused our effort on three compounds, C26, C32, and C34 with IC50 of less than 20 μM (Fig. 3d and Supplementary Table 6). Given that C32 and C34 share a similar structure (Fig. 3d), and C32 has a lower IC50 (Supplementary Table 6), C34

was not pursued in further studies. To further understand the structure-activity relationships, focused collections of C26 and C32 analogs were strategically selected and obtained for testing with split- and linked-luc assay (Supplementary Table 7). Candidates that showed positive results were analyzed further to generate inhibitory efficiency curves with multiple doses (Fig. 3e). Selected analogs for both C26 and C32 had better efficacy than their parent compounds (Fig. 3e).

Co-immunoprecipitation assay (Co-IP), which is a commonly used standard test to determine protein-protein interaction, was next employed to validate the candidates. Lysates of breast cancer cell line SCP28, a single cell-derived subline from the MDA-MB-231 TNBC cell line[25], was immunoprecipitated with anti-MTDH antibody alone or together with inhibitors (Fig. 3f and Extended Data Fig. 3e). The samples were then incubated with Protein-A/G beads to pull down MTDH, followed by western blot analysis to detect SND1. In such co-IP experiment, MTDH-WT but not MTDH-MT peptide blocks MTDH-SND1 interaction (Extended Data Fig. 3e). When C26s and C32s were tested in the Co-IP assay, both series of compounds significantly block MTDH-SND1 interaction, with strongest inhibitory effects achieved by C26-A2 and C26-A6 (Fig. 3f). Taken together, with multiple screening and validation platforms, we obtained two classes of compounds, C26s and C32s, that inhibit MTDH-SND1 interaction.

C26s block SND1 pocket to disrupt MTDH-SND1 complex

Next, we asked how C26s and C32s disrupt MTDH-SND1 interaction. According to our previous findings[12], we hypothesized that the compounds may occupy either one or both of the two hydrophobic pockets on SND1 to inhibit MTDH-SND1 interaction. To test this hypothesis, we first aimed to determine if the compounds bind to SND1. To this end, the interaction domain of SND1 was purified and thermal melt assay was performed. The assay is dependent on the interaction of a hydrophobic fluorophore and core hydrophobic residues within a protein. At low temperatures when the protein is well folded and the hydrophobic residues are buried within the protein core, no fluorescence signal is observed. With increasing temperature, the protein starts to unfold and hydrophobic areas are exposed, which can then bind to the fluorophore, leading to increased fluorescence signal. However, if there are compounds in the solution that bind to the protein, significant increases or decreases (+/− 2°C and above) in the melting temperature can be observed[26]. Two C26 analogs and three C32 analogs that showed best efficacy described above (Fig. 3e) together with MTDH-WT/MT peptides (as positive/negative controls) were subjected to the assay. MTDH-WT but not MT peptide caused significant melting temperature change (Fig. 4a), validating the feasibility of the assay. Interestingly, only the C26 analogs, but not the C32 analogs induced significant temperature change (Fig. 4a). Moreover, the temperature changes induced by C26s were dose dependent (Extended Data Fig. 3f). These data indicate direct binding of C26s to SND1.

To validate the interaction between C26s and SND1, and to quantify the binding affinity, MicroScale Thermophoresis (MST) assay was employed. MST detects changes in the hydration shell, charge or size of molecules by measuring changes of the mobility of molecules in a microscopic temperature gradient[27,28]. To perform the assay, purified SND1

proteins that were labeled with Monolith NT™ His-tag RED-tris-NTA dye and incubated with C26s or WT/MT MTDH peptides. As positive and negative controls, MTDH-WT and MT peptides showed positive and negative SND1 binding respectively (Extended Data Fig. 3g). As expected, both C26-A2 and A6 showed positive SND1 binding (Fig. 4b). Moreover, C26-A2 and A6 have similar or even slightly better binding affinity than MTDH-WT peptide as evidenced by K_D values (Supplementary Table 8). Overall, the results confirmed that C26-A2 and A6 (Fig. 4c) interact with SND1 to disrupt MTDH-SND1 interaction.

The thermal melt assay and MST assay mentioned above only suggest the binding of C26s and SND1, without providing information about binding sites. To further investigate how C26s bind to SND1 to block the interaction, we co-crystalized SND1 with C26-A2 or A6 and the structures were determined at 2.7 Å resolution (Supplementary Table 9). Our previous study indicated that two tryptophan residues (W401 and W394) of MTDH inserted into two pockets (pockets 1 and 2) on SND1 to mediate the interaction between two proteins (Extended Data Fig. 4a)[12]. The co-crystal structural data revealed that both C26-A2 and A6 bind to a small groove on the SND1 protein surface flanked by residues Arg255, His279, Asn281, Arg259, Ile284, Leu287, and Leu256 (Fig. 4d–f). The compounds flank the side chain of Arg255, and the interaction is stabilized by two direct hydrogen bonds between atoms N and N2 of the triazolopyridinamine (C26-A2) or methyltriazolopyridinamine (C26-A6) moiety and Arg255 NE and NH2, respectively (Fig. 4e,f). The chloromethoxybenzene moiety is sandwiched between atoms CA, CB and CG of Arg255 and residues Asn281 to Ile284 and thus occupies the position of the Trp401 side chain from the MTDH peptide according to our previous study (Fig. 4e,f and Extended Data Fig. 4b,c)[4,12]. The chlorine atom points towards Ile284 N, whereas the methoxy group is oriented towards the solvent forming a hydrogen bond between the oxygen atom and Asn281 ND2. The triazolopyridinamine (C26-A2) or methyltriazolopyridinamine (C26-A6) moiety is sandwiched between Leu287 from the corresponding chain and Ile284 from an adjacent molecule (Fig. 4e,f). Overall, co-crystal structure analysis confirmed that C26-A2 and C26-A6 bind to the same SND1 pocket occupied by W401 of MTDH in an almost identical manner (Extended Data Fig. 4d). As such, C26-A2 and A6 compete with MTDH to interact with the same pocket, thereby disrupting the MTDH-SND1 complex.

C26s inhibit breast cancer progression and metastasis

Next, we tested whether C26-A2 and A6 could inhibit breast cancer progression. First, Caco-2 cell based permeability test[29] confirmed that both compounds are highly permeable (Extended Data Fig. 5a). Next, SCP28 breast cancer cells that were engineered to express split- or linked-luciferase reporter were treated with C26-A2 and A6. Consistent with results from cell free system (Fig. 3e), both compounds inhibit split-luc activity in living cells in a dose dependent manner without significantly affecting linked-luc activity (Fig. 5a). Moreover, the blocking efficiency was not significantly changed 5 days after the addition of the compounds (Fig. 5b), suggesting the stability of the compounds in cells.

Next, *PyMT;UBC-Cre*[ERT+/−]*;Mtdh*^{fl/fl} tumor cells: 1) with or without *Mtdh* pre-depletion; 2) with or without endogenous *Snd1* knockdown; or 3) in combination were employed for tumorsphere assay followed by the compound treatments. C26-A2 and A6 inhibited spheres

formed by *PyMT;UBC-Cre^(ERT+/−);Mtdh^(fl/fl)* wild type tumor cells (Fig. 5c), however, they had no effects on the spheres with *Mtdh* KO or *Snd1* KD (Fig. 5d–g). The results were confirmed using *C3* and *Wnt;UBC-Cre^(ERT+/−);Mtdh^(fl/fl)* tumorspheres (Extended Data Fig. 5b–e). Taken together, these findings confirmed that the anti-tumor effect of C26-A2 and A6 is dependent on their specific effect on blocking MTDH-SND1 interaction.

To test the *in vivo* blocking effect of C26-A6 on MTDH-SND1 interaction, mice with SCP28 tumors that stably express split-luciferase components were treated with vehicle, 0.25 mg or 0.5 mg of C26-A6 via tail-vein injection followed by bioluminescence imaging. The result indicated that C26-A6 blocks MTDH-SND1 interaction *in vivo* in a dose-dependent manner (Extended Data Fig. 6a,b).

Next, established orthotopic PyMT tumors[4] were treated with vehicle or C26-A6 (Fig. 6a). Continuous treatment of C26-A6 significantly inhibited primary tumor growth and spontaneous lung metastasis (Fig. 6b–d, and Extended Data Fig. 6c), while having no significant hematologic, GI tract, and liver toxicity (Extended Data Fig. 6d–h). The results were confirmed with SCP28 xenograft tumor model in NSG mice (Extended Data Fig. 7a–c). Consistent with its tumor-suppressive effects, C26-A6 treatment reduces tumor proliferation and induces tumor apoptosis (Extended Data Fig. 7d,e). Similar therapeutic effects were also observed in a TNBC patient-derived xenograft (PDX, HCI-001) model[30] (Extended Data Fig. 7f–i).

To confirm at the molecular level that C26-A6 targets the MTDH-SND1 complex to suppress breast cancer progression, *PyMT;UBC-Cre^(ERT+/−);Mtdh^(fl/fl)* mice with tumors were treated with vehicle, Tmx, and C26-A6, followed by next-generation RNA sequencing (NGS). Non-supervised clustering based on global gene expression data indicated that Tmx and C26-A6 groups cluster together (Extended Data Fig. 7j), suggesting that *Mtdh* acute KO and C26-A6 treatment have similar effect on gene expression in tumors. Moreover, gene set enrichment analysis (GSEA) showed that Tmx treatment upregulated and downregulated genes are sharply enriched positively or negatively in C26-A6 tumors, respectively (Fig. 6e, left and middle panels), suggesting *Mtdh* acute KO and C26-A6 treatment regulate similar genes and pathways in breast tumors. To provide a better understanding of how C26-A6 exerts its tumor suppressive function, C26-A6 downregulated genes in comparison with vehicle were employed for Ingenuity Pathway Analysis (IPA). A significant enrichment of "Cell Death and Survival", "Cell Cycle", and "DNA repair" molecular and cellular functions was observed (Extended Data Fig. 7k). Genes involved in cell survival and viability were decreased, whereas genes involved in apoptosis were increased (Extended Data Fig. 7l) in C26-A6 treated tumors, which is similar as what we found in SND1-dependent signature during chemotherapy (SND1_CPT_UP)[4]. Furthermore, SND1_CPT_UP signature that negatively enriched in MTDH-SND1 interaction deficient tumors[4], is also down regulated upon C26-A6 treatment (Fig. 6e, right). Taken together, these results confirm that C26-A6 targets MTDH-SND1 interactions to exert a global gene expression changes, leading to inhibition of breast cancer progression.

To obtain insights into the molecular mechanism underlying C26-A6 treatment-induced reduction of cell viability and increase of apoptosis, we employed *in vitro* sphere assays.

PyMT tumorspheres are more susceptible to C26-A6 treatment than normal mammary epithelial cells (MECs) (Extended Data Fig. 8a). 200 μM C26-A6 treatment significantly reduced survival and induced G2/M cell cycle arrest in PyMT tumorspheres, but not in normal MEC spheres (Extended Data Fig. 8b–i and Supplementary Fig. 1). To further explore the downstream effectors of tumor-suppressive response to C26-A6, we performed GSEA analysis of PyMT tumor with or without C26-A6 treatment. The cell cycle and cell survival relevant signatures, E2F_TARGETS, G2M_CHECKPOINT, and MYC_TARGETS were significantly enriched in the control (vehicle) group compared to the C26-A6 treated group (Extended Data Fig. 9a). Leading edge analysis of these enriched signatures results in a few downstream candidates, including *Cdc20*, *Mcm6*, *Mcm5, Plk1*, *Mcm2* and *c-Myc*, that are significantly down-regulated upon C26-A6 treatment (Extended Data Fig. 9b). Western blot analysis of the PyMT tumorspheres showed that, among these candidates, Cdc20, Plk1, and c-Myc were down-regulated by C26-A6 treatment (Extended Data Fig. 9c), an observation that was also confirmed using SCP28 tumor samples (Extended Data Fig. 9d,e). Interestingly, RNA-sequencing data of the normal MEC spheres did not reveal comparable signature enrichment or gene expression changes as in tumor samples (Extended Data Fig. 9f–h). Collectively, the data suggested Cdc20, Plk1, and c-Myc as possible downstream targets that mediate the effect of MTDH-SND1 inhibition on inducing tumor-intrinsic cell cycle arrest and apoptosis.

Next, to further validate that the anti-tumor effect of C26-A6 depends on its on-target effects by disrupting MTDH-SND1 complex, *PyMT;UBC-Cre^{ERT+/−};Mtdh^{fl/fl}* tumor cells with *Mtdh* depletion or with endogenous *Snd1* KD were employed for the similar assay as in Fig. 6a. The result indicated that C26-A6 did not further inhibit tumor growth or metastasis in the models with MTDH KO or SND1 KD (Fig. 6f–k, and Supplementary Fig. 2). Likewise, MTDH or SND1 KD abolished the C26-A6 treatment-induced primary tumor inhibition or metastasis reduction in SCP28 tumor models (Extended Data Fig. 10a–c).

To exclude the possibility that the lung metastasis reduction upon C26-A6 treatment was due to the smaller primary tumor, we performed tail vein injection of PyMT tumor cells to form experimental lung metastasis in FVB mice. 3 days later, mice were divided randomly into two groups and treated with vehicle or C26-A6 respectively (Fig. 6l). Five weeks of C26-A6 treatment significantly suppresses lung metastasis (Fig. 6m). Similarly, C26-A6 also dramatically inhibits experimental lung metastasis of SCP28 cells (Extended Data Fig. 10d,e). The primary tumor growth and metastasis-suppressive role of C26-A6 was further validated with additional breast cancer models, including the SUM159-M1a lung-metastatic human breast cancer cell line in NSG mice[31,32] and 4T1 mouse mammary tumor models in immunocompetent Balb/c mice (Extended Data Fig. 10f–l). Taken together, the data revealed that C26-A6 blocks MTDH-SND1 interaction to inhibit breast cancer progression and metastasis.

MTDH-SND1-targeting sensitizes breast cancer to chemotherapy

Given that MTDH promotes chemoresistance[2], we hypothesize that MTDH-targeting could sensitize breast cancer to chemotherapy. To test this, *PyMT;UBC-Cre^{ERT+/−};Mtdh^{fl/fl}* mice with established tumors were treated with Tmx and paclitaxel alone or in combination (Fig.

7a). Acute loss of *Mtdh* by Tmx treatment significantly reduces primary tumor growth and lung metastasis (Fig. 7b,c). Importantly, Tmx+paclitaxel combined treatment dramatically reduces primary tumor growth and lung metastasis to a degree that is superior to paclitaxel or Tmx treatment alone (Fig. 7b,c).

Chemotherapies are commonly applied to the treatment of triple-negative breast cancer (TNBC). We analyzed 363 subjects with TNBC, who were treated with chemotherapy after surgeries (Supplementary Table 10). Primary tumor samples were surgically removed before chemotherapy and were used to measure *MTDH* expression. Patients with *MTDH*-high expressing tumors had significantly worse overall, relapse-free, and lung metastasis-free survival (Fig. 7d) after surgery and chemotherapy. This finding indicates the possibility to target MTDH in human patients in order to sensitize the TNBC patients to chemotherapy.

Based on these findings, we directly tested whether pharmacological inhibition of MTDH-SND1 can synergize with chemotherapy to improve treatment outcome in mouse models. Similar to experiments using genetic depletion *Mtdh* (Fig. 7b,c), C26-A6+paclitaxel has significantly better efficacy in inhibiting SCP28 primary tumor growth and lung metastasis than C26-A6 or paclitaxel treatment alone (Fig. 7e,f).

Next, we investigated the efficacy of the treatments in suppressing metastatic colonization. To this end, Balb/C mice were injected with 4T1 mouse mammary tumor cells, which mimic TNBC[33], via tail-vein and were subjected to the same treatment regime as above three days later. Consistently, C26-A6+paclitaxel significantly inhibited lung metastasis more than either treatment alone (Fig. 7g). Furthermore, mice with C26-A6+paclitaxel treatment had the best survival rate (Fig. 7h).

Lastly, to mimic the clinical scenario of adjuvant chemotherapy following surgical removal of the primary tumors, SCP28 mammary tumors were removed when they reached 5 mm in diameter, the mice were then randomly separated into four groups and subjected to the different treatment regimens as above. Again, C26-A6+paclitaxel treatment achieved the more effective reduction of lung metastasis and overall survival (Fig. 7i,j), suggesting targeting MTDH-SND1 complex together with chemotherapy could significantly improve the treatment outcome for breast cancer. To further evaluate if the treatment could result in the shrinkage of established macrometastases, we performed tail vein injections to generate 4TO7 lung metastases bearing mice. The mice were randomized into four groups of 6 mice each when macrometasetases were well-established, as evidenced by robust BLI signals in the lungs (Fig. 8a,b). The mice were then treated with vehicle or paclitaxel and C26-A6 alone or in combination, and the metastasis progression was monitored by BLI. Although paclitaxel or C26-A6 treatment alone slowed down metastatic growth, these monotherapies did not result in metastasis shrinkage (Fig. 8c). However, three mice in C26-A6+paclitaxel group have stabilized disease and one mouse has obvious metastasis shrinkage, leading to significantly improved survival rate (Fig. 8c,d). More importantly, consistent with our results showed above (Extended Data Fig. 6d–h), C26-A6 was well tolerated by the mice and did not further enhance the chemotherapy toxicity when combined with paclitaxel (Fig. 8e–h). These data suggest that C26-A6 combined with chemotherapy may have clinical benefit in metastatic breast cancer patients.

Discussion

In this study, we evaluated the therapeutic potential of targeting MTDH-SND1 complex using a combined genetic and pharmacological approach. The inducible conditional *Mtdh* KO mouse and cell line models provided a relevant pre-clinical model to mimic MTDH-targeting in an autochthonous and immunocompetent tumor development setting and allowed more accurate assessment of its therapeutic benefit in late tumor development stages. Importantly, acute pharmacological and genetic inhibition of MTDH revealed robust and consistent global gene expression changes that were not easily discernable in our previous studies using constitutive MTDH-KO mouse or cell line models. Our data provided essential proof-of-concept evidence that MTDH is a suitable target for the treatment of established breast cancer and potentially other cancers. Furthermore, we identified a series of first-in-class small chemical compounds that achieved robust therapeutic effects by disrupting MTDH-SND1 interaction.

Protein-protein interactions (PPIs) are critical for all the biological processes including tumorigenesis and cancer progression[34,35]. Despite the importance of PPIs in disease development, targeting PPI was initially considered to be impossible due to the large, flat, and featureless interaction interface[36]. However, with recent breakthroughs in technology development, high resolution structural studies revealed that not all residues at the PPI interface were critical, but rather that small "hot spots" conferred most of the binding energy[37–39], paving the path to the recent success of PPI inhibitor development[40–44]. Consistent with this notion, our previous structural biology study revealed that MTDH-SND1 interaction was critically reliant on several key residues of MTDH and SND1, and that such interactions were potentially amenable to disruption by small chemical compounds[12].

Co-crystal structures of the C26s-SND1 complex confirmed the SND1 binding of C26s and their competition with MTDH to disrupt the complex (Fig. 4 and Extended Data Fig. 4). However, both of the two tested C26 analogs block the same SND1 pocket and leave another pocket free (Fig. 4e,f). Additional screens focusing on discovery compounds that target the other pocket of SND1 need to be performed in the future. Given the short distance (~15 Å) between the two pockets of SND1[12], candidates that block another pocket could be crosslinked with C26-A6 with an appropriate length of spacer. The resulting compounds that bind to two pockets simultaneously are expected to have much higher MTDH-SND1 disruption ability.

Functional studies of C26s suggested potential tumor suppressive role of this structural class of compounds (Figs. 5–7). Moreover, C26-A6, which is the best analog of C26, is very tolerable *in vivo* with minimal toxicity (Fig. 8 and Extended Data Fig. 6). Considering the high tolerability *in vivo* and the compound's solubility, we determined to use highest dose we can achieve (15 mg/kg) for the treatment experiments. C26-A6 treatment alone or in combination with chemotherapy dramatically suppresses breast cancer progression and metastasis (Figs. 6–8), consistent with gene expression analyzing showing the pro-survival and anti-apoptosis role of MTDH in cancer cells under stressful situations, such as chemotherapy.

Target specificity of the drug is critical for clinical application of novel therapeutic compounds. To this end, we provided multiple lines of evidence showing that the tumor-suppressive effect of C26-A6 is due to its on-target effects: phenotypically, we have developed tumor models with MTDH-KO or SND1-KD and then treated with C26-A6. In this experiment setting, we did not observe any further tumor inhibition upon C26-A6 treatment (Fig. 6), suggesting that C26-A6 targets MTDH-SND1 to exert its tumor inhibition function. At the molecular levels, co-crystal structure shows that C26 series compounds occupy the essential pocket in SND1 to block its interaction with MTDH (Fig. 4). Moreover, RNA sequencing data together with the gene set enrichment analysis suggested that C26-A6 treatment and MTDH-KO or SND1 silencing alter the exact same set of pathways (Fig. 6 and Extended Data Fig. 7). Taken together, we believe that the tumor- and metastasis-suppressive effects of C26-A6 treatment is due to its on-target effect on blocking the MTDH-SND1 complex and its downstream targets. Collectively, our results underscore the feasibility and therapeutic potential of targeting the MTDH-SND1 complex for the treatment of breast cancer and establish the C26 series as promising candidates for further development as a new first-in-class cancer therapeutic agent.

Methods

Animal models

All procedures involving mice and experimental protocols were approved by the Institutional Animal Care and Use Committees (IACUC) of Princeton University. According to our approved IACUC protocol (1881–20), the primary humane endpoint of tumor burden for an individual mouse is 20 mm in any dimension or a total volume of 4000 mm^3 for mice with multiple tumors. Mice were euthanized before exceeding the limit of tumor burden in this study. In our facility, mice were maintained at 20–22°C with 14 h:10 h light:dark cycles at 40–70% relative humidity. The *Mtdh$^{fl/fl}$* ES cell lines generated by *Mtdh* targeting vector (CSD48311) was obtained from the KOMP Repository. The ES cells were injected into the C57BL/6 blastocysts followed by confirmation of germline transmission. *Mtdh$^{fl/fl}$* mice were crossed with FLPe mice to remove the selection marker in the vector. Genotyping (Forward primer: CCCACCCCGCTTTGACCAAATAC; Reverse primer: GTGCCACCACTGCCCAGCTTC) was performed to identify positive mice before they were crossed to other strains that were indicated in each experiment. FLPe (Stock No. 003946), MMTV-PyMT (Stock No. 002374), MMTV-WNT1 (Stock No. 002934), C3 (Stock No. 013591), UBC-Cre^{ERT2} (Stock No. 007001), FVB (Stock No. 001800), Balb/C (Stock No. 000651), Athymic nude (Nude) (Stock No. 002019), and NOD Scid Gamma (NSG) (Stock No. 005557) were obtained from Jackson Laboratory. Mice in C57BL/6 background were backcrossed to FVB for at least 10 generations to change the background. For spontaneous tumor models, the mice were randomized and matched by tumor size rather than time of growth before we started the treatment. For xenograft/allograft studies, 8-weeks immunocompromised NSG, Nude or immunocompetent FVB or Balb/C females were used. Injections were performed as previously described[32]. The mice were randomized as indicated in each specific experiment before we started the treatments. For Tamoxifen (Tmx) and Paclitaxel (Pac) treatments, mice were injected with 60 mg/kg and 20 mg/kg via i.p. respectively. For C26-A6 treatments, mice were injected with 15 mg/kg via i.v.

Primary tumors were considered established when they became palpable for 2 consecutive weeks. The tumors were measured by calipers for calculation of tumor volumes (length x width^2/2). For cell lines that are stably labeled with a firefly luciferase expressing vector, lung metastases were monitored by bioluminescent imaging (BLI) and images were processed with Living Image 3D Analysis (version 1.0). For PDX treatment, fresh TNBC patient-derived xenograft (PDX, HCI-001)[30] was chopped into ~1–2 mm in diameter cubes and inoculated into 8-week NSG females. One day after inoculation, the mice were randomized and treated with vehicle or C26-A6.

Generation of TNBC cohort and expression determination

The generation of TNBC cohort has been detailed described in our previous studies[7,45]. As noted, our study was approved by the independent ethics committee/institutional review board of FUSCC (Shanghai Cancer Center Ethics Committee). All patients gave their written informed consent before inclusion. 386 patients were selected, and RNA sequencing was performed on 245 samples. HTA 2.0 array sequencing was performed on the other 141 samples. Detailed information of HTA data was described in our previous article[46,47]. We utilized Combat ("ComBat" function in R) to adjust batch effects between the RNA-seq and HTA array datasets. To calculate the prognostic efficacy of *MTDH* on overall survival, relapse and lung metastasis in the TNBC patients with chemotherapy, we first chose the optimal cutoff value ("cutp" function in R) to classify the expression of *MTDH* into low and high expression subtypes in each prognostic calculation. Afterwards, survival analysis was performed as previously described[7].

Cell culture

SUM159-M1a was derived from SUM159 breast cancer cell line[31]. HEK293T (CRL-3216) and 4T1 (CRL-2539) were obtained from American Type Culture Collection. SCP28, 4TO7, and H29 were obtained from Dr. Joan Massagué. *PyMT;UBC-Cre$^{ERT+/−}$;Mtdh$^{fl/fl}$*, *C3;UBC-Cre$^{ERT+/−}$;Mtdh$^{fl/fl}$*, and *Wnt;UBC-Cre$^{ERT+/−}$;Mtdh$^{fl/fl}$* cell lines were generated in this study. SCP28, 4T1,4TO7, HEK293T, and the generated cell lines were grown in DMEM supplemented with 10% FBS and pen/strep. SUM159-M1a cells were culture with F12 media supplemented with 10% FBS, 10 μg/ml Insulin, 20 μg/ml EGF and pen/strep. H29 was grown in the same media supplemented with 2 μg/ml puromycin, 300 μg/ml G418 and 1 μg/ml doxycycline. All cells were regularly checked for *Mycoplasma* and authenticated.

Cloning, viral production and transduction of cell lines

To generate plasmids that express split- and linked-luciferase components, plasmids that express human *MTDH* and *SND1* from our previous studies[2,8] were used as template. Firefly luciferase plasmid (pGL3, Promega, Cat#E1751) was also employed as template. Firefly luciferase was split into N-terminal (NLuc: 1–416aa) and C-terminal (CLuc: 398–550aa) as previously reported[21]. SND1 (16–339aa) was cloned and fused to N-terminal of NLuc with 3 repeats of GGGS as a linker. Similarly, MTDH (386–407aa) was cloned and fused to C-terminal of CLuc with 3 repeats of GGGS. SND1-NLuc and CLuc-MTDH flanked by *BamH 1* and *Not 1* restriction sites were inserted into pcDNA3.1 and pRVPTO (retrovrial) vectors. Human influenza hemagglutinin (HA) tag was fused to SND1-NLuc and Myc tag was fused to CLuc-MTDH. For linked-luciferase, NLuc and CLuc were

linked with 3 repeats of GGGS, flanked by the same restriction sites, and inserted into the same vectors. shRNAs targeting human *MTDH*[2] and *SND1*[8] was described in our previous studies. shRNAs targeting mouse *Snd1* was purchased from Sigma (TRCN0000295753) and validated in our previous study[4,12]. Mouse wild type full length MTDH and SND1 interaction deficient mutant MTDH-13D (MTDH-W391D) was reported in our previous study[4]. All plasmids were sequenced and confirmed for accuracy. To generate SCP28 cell line that stably express split- and linked-luciferase components, retroviral vectors generated above were transfected into the H29 packaging cell line. Detailed procedure was described in our previous study[32].

Generation of tumor cell line from inducible *Mtdh* KO mice

PyMT;UBC-Cre[ERT+/−]*;Mtdh*^{fl/fl}, *C3;UBC-Cre*[ERT+/−]*;Mtdh*^{fl/fl}, and *Wnt;UBC-Cre*[ERT+/−]*;Mtdh*^{fl/fl} tumor cell lines were generated as following: *FVB-PyMT/C3/Wnt;UBC-Cre*[ERT+/−]*;Mtdh*^{fl/fl} mice that have primary tumors around 5 mm in diameter were sacrificed. The primary tumor was dissected and plated into 10 cm dished. Two days later, floating tissues were washed off with culture media and attached cells were further cultured with fresh media to become stable cell lines.

Immunoprecipitation (IP) and western blotting (WB) analysis

For IP experiment, samples were prepared as previously described[32]. 100 μl of the supernatant was transferred to a new tube as input, and the rest was incubated with 2 μg of IgG, anti-Myc (Santa Cruz, SC-40), or anti-MTDH (ThermoFisher, 40–6500) (as indicated in each experiment) overnight at 4°C (small chemical compounds may be added at this step as indicated in each experiment). The rest standard IP procedures were performed as previously noted[32]. For WB analysis, samples were resolved with SDS-PAGE gel and immunoblotted with HA (Sigma, 11867431001), β-actin (Sigma, A1978), Cdc20 (Cell signaling, 14866S), Plk1 (Cell signaling, 4513T), c-Myc (Novus Biologicals, NB600–302), Mcm2 (Cell signaling, 3619T), Mcm5 (ProteinTech, 67049–1-Ig), and Mcm6 (ProteinTech, 13347–2-AP) antibodies with 1:1000 dilution.

Immunohistochemistry (IHC) staining.

Paraffin-embedded primary tumor samples were processed as previously noted[32]. Slides were incubated at 4°C overnight with Ki67 (Leica Biosystem, Ki67-MM1-L-CE-S), cleaved caspase-3 (Cell signaling, 9661S), Cdc20 (Cell signaling, 14866S), Plk1 (Cell signaling, 4513T) or c-Myc (Novus Biologicals, NB600–302) antibodies with 1:100 dilution. Following washes with PBS, slides were stained as described before[32]. Images were taken with Carl Zeiss Zen (version 3.0) and processed with ImageJ (bundled with Java 1.8.0_172).

NGS and GSEA

For next-generation sequencing (NGS), age matched *PyMT;UBC-Cre*[ERT+/−]*;Mtdh*^{fl/fl} female mice with similar tumor burdens were treated and the tumors were collected. For spheres, 100k mammary epithelial cells were seeded into each well of the 6-well low attachment plates. Five days after seeding, spheres were formed and were treated with vehicle or 200

μM of C26-A6 for another one week and the spheres were harvested. Total RNA samples were prepared from the tumors or spheres using RNAeasy kit (Qiagen). The RNA-seq libraries were prepared, examined and raw reads were processed as previously described[7,45].

We used GSEA v3.0 for gene set enrichment analysis[48,49]. Normalized gene expression data were pre-ranked based on the differences of expression (fold changes). SND1_CPT_UP signature was extracted from our previous study[4].

Luciferase-based screening

Seed HEK293T cells on 3×15 cm dish at 18–24 hr before transfection with 7–8X10^6 cells per dish targeting 70–80% confluence when start transfection. 20 μg of pCDNA3.1-SND1-NLuc, pCDNA3.1-CLuc-MTDH, or 2 μg of pCDNA3.1-NLuc-CLuc plasmids that described above were transfected to each dish. 72 hr after transfectionthe cells were lysed with 5 ml of luciferase lysis buffer (2 mM EDTA, 20 mM DTT, 10% glycerol, 1% Triton X-100, 25 mM Tris base, adjusted to pH7.8 with H_3PO_4) at 4°C for 20 min. The protein lysates were centrifuged at 13,000 rpm for 10 min, and the supernatant were collected.

For small chemical compound screening, white, flat-bottom, solid 384-well plates were used. Compounds were added into each well as 0.1 μl of 10 mM DMSO solution (or same amount of DMSO, serve as control). The first and last columns were free, and MTDH wild type (PNSDWNAPAEEWGNW) or mutant (PNSDANAPAEEAGNW) peptides were added as positive and negative controls right before screening. Same amount of MTDH-CLuc and SND1-NLuc were pre-mixed at 4°C for 30 min to generate split-luc. 5 μl of split- or linked-luc was added into each well. 15 μl of luciferase assay buffer (25 mM Glycylglycine pH 7.8, 15 mM K_3PO_4 pH 7.8, 15 mM $MgSO_4$, 4 mM EGTA, 2 mM ATP added just before use, 10 mM DTT added just before use and 1 mM D-Luciferin added just before use) was then added into each well to get a 20 μl reaction system with 50 μM of compounds (peptides) in each well. The plates were incubated at 4°C for 1 hr and luciferase activity at each well was measured.

The inhibitory efficiency of each compound was calculated as following: (signal at DMSO well – signal at compound well) / signal at DMSO well. MTDH wild type or mutant peptide in each plate was served as positive and negative controls to monitor the data quality of each plate.

FRET- based screening

To perform FRET assay, purified CFP-MTDH (386–407aa) and TC-SND1 (16–339aa) proteins were reconstituted in FRET buffer (25mM Tris-HCl pH8.0, 150 mM NaCl, 3mM DTT, 2% DMSO). 384-well plate (Corning, black, flat bottom. Catalog number 3575) was used for this assay and the compounds/peptides were distribute into each well as above. 0.065 μl of CFP-MTDH was added to 8.9755 μl of FRET buffer, and then transferred the mixture to each well. Incubate the plate for 5 min at room temperature, avoid light. 1.86 μl of TC-SND1, 0.024 μl of FIAsH-EDT2 Labeling reagent (TC-FlAsH™ II In-Cell Tetracysteine Tag Detection Kits, Cat#T34561) together with 8.9755 μl of FRET buffer was mixed and then added to each well. The plate was measured with excitation weave length of 450 nm and emission weavelength of 495 nm and 535 nm.

The inhibitory efficiency was calculated as following: After subtracting the value of DMSO background, the emission of CFP-MTDH at 495 nm is considered as D, the emission of TC-SND1+FlAsH is A, the emission of CFP-MTDH + TC-SND1+FlAsH mixture is DA, the efficiency is calculated as 1-(DA-A)/D. Similarly, MTDH wild type or mutant peptide in each plate was served as positive and negative controls to monitor the data quality of each plate.

Candidate selection

Singleton small molecule library was screened with split-luciferase for two rounds (R1 and R2) (Supplementary Table 2). The candidates showed inhibitory efficiency equal or greater than 0.4 were chosen and repeated twice with split-luc, linked-luc, and FRET assay. The average of inhibitory efficiency from each assay was calculated (average inhibitory of split-luc was consider as R3) (Supplementary Table 3). Compounds were selected if they fall into any of the following criteria (Supplementary Table 4): 1) The inhibitory efficiency in R1 and R2 were normalized with the linked-luc average value. The candidates still gave greater than 0.4 inhibitory efficiency after normalization in both rounds (R1/Linked-luc avg.>0.4)&(R2/Linked-luc avg.>0.4); 2) The inhibitory efficiency in R1 and R3 were normalized with the linked-luc average value. The candidates still gave greater than 0.4 inhibitory efficiency after normalization in both rounds (R1/Linked-luc avg.>0.4)&(R3/Linked-luc avg.>0.4); 3) The inhibitory efficiency in R2 and R3 were normalized with the linked-luc average value. The candidates still gave greater than 0.4 inhibitory efficiency after normalization in both rounds (R2/Linked-luc avg.>0.4)&(R3/Linked-luc avg.>0.4); 4) Only the candidates with the inhibitory efficiency between –0.2 to 0.2 in linked-luc assay were considered. The candidates were selected if they have split-luc inhibitory efficacy greater than 0.4 in both: a) R1 and R2; b) R2 and R3; c) R1 and R3; 5) The candidates showed inhibitory efficiency greater than 0.06 in both rounds of FRET assays; 6) The candidates share structure similarity with the above selected ones. 52 compounds were selected with these criteria (Supplementary Table 5).

The list of candidates was confirmed with split- and linked-luc assay and FRET assay again. Candidates were selected if they fall into any of the following criteria: 1) The inhibitory efficiency of split-luc is greater than 0.9; 2) The inhibitory efficiency of split-luc that normalized with linked-luc is greater than 0.2; or 3) Inhibitory efficiency in FRET assay is greater than 0.2. 12 candidates were selected after filter with these criteria (Supplementary Table 6).

Thermal Melt assay

0.1 mg/ml of purified SND1 (16–339aa) protein together with 5-fold of Sypro Orange dye was added into assay buffer (20 mM HEPES, 150 Mm NaCl, pH 7.0). 250 μM of MTDH wild type/mutant peptides, indicated amount of compounds or same amount of DMSO was then added into each reaction. Temperature increased from 25°C to 95°C and fluorescence signal was measured. T_m max = T_m max (compound) - T_m max (DMSO)

Microsacle Thermophoresis (MST) assay

To perform MST assay, 150 nM purified SND1 (16–339aa) protein was labeled with 50 nM of RED-tris-NTA dye. Monolith NT.115 Instrument using the RED detector was employed. MTDH wild type/mutant peptides were screened in a twelve point two-fold serial dilution with concentrations ranging from 50 μM to 24.4 nM. The C26s compounds were screened in a twelve point three-fold serial dilution with concentrations ranging from 0.5 mM to 2.82 nM.

The assay was performed in buffer containing: 20 mM Hepes pH 7.0, 150 mM NaCl and 10 % Glycerol. After a 30 min incubation with the respective compound and 5 min centrifugation at 14000 rpm, the samples were loaded into MonolithTM NT.115 Series Standard Treated Capillaries. The MST analysis was performed using LED Power: 60% and MST Power: 40%. The normalized fluorescence F_{norm} measures mainly this concentration ratio, plus a temperature dependence of the dye as noted before[50]. Concentrations on the x-axis are plotted in nM. A K_D was determined with the MO.Affinity Analysis Software v2.2.4.

Co-crystal structure analysis

The SND1 construct used for crystallization comprises residues 16 to 330 of the wild type SND1 protein with two loops being deleted (residues 65 to 70 and residues 235 to 239). Crystals of SND1 in complex with C26-A2 and C26-A6 were obtained using sitting drop vapour diffusion set-ups. SND1 at a concentration of 18.08 mg/ml (20 mM Hepes, 150 mM NaCl, 1 mM TCEP, pH 7.5) was pre-incubated with 2.5 mM (5.1-fold molar excess) of C26-A2 or A6 (150 mM in DMSO) for 1 h. 1 μl of the protein solution was then mixed with 1 μl of reservoir solution (0.10 M MES/NaOH, pH 6.20, 0.90 M Na$_3$-Citrate) and equilibrated at 20°C with 0.4 ml of reservoir solution. Well diffracting crystals appeared within 4 days and grew to full size over 7 days.

A complete 2.7 Å data set of a SND1/C26-A2 (PDB ID: 7KNW) or A6 (PDB ID: 7KNX) crystals were collected at a Bruker Liquid Metal Jet X-ray Source equipped with HELIOS MX optics. Molecular replacement was done using a previously determined structure of SND1 as starting model[12]. Several rounds of alternating manual re-building and refinement with REFMAC5 resulted in the final model. The model has excellent stereochemistry with only eight outliers in a Ramachandran plot, justifiable by electron density. Structural images were presented by PyMol (version 2.3.3).

C26s cell permeability test

The cell permeability of C26-A2 and A6 were determined with monolayer of Caco-2 cells with both the apical-to-basolateral (A-to-B) and basolateral-to-apical (B-to-A) directions by Absorption Systems LLC Detailed protocol can be found in previous study[51].

Tamoxifen, C26-A6 and Paclitaxel for *in vivo* treatment

Tamoxifen (Tmx) (Sigma-Aldrich, T5648) was reconstituted with corn oil (Sigma-Aldrich, C8264) at 20 mg/ml. After 1 hr of shaking at 37°C the solution is ready for use. For

the treatment, indicated mice were injection with 60 mg/kg of the solution via i.p. for 5 constitutive days.

C26-A6 was synthesized by WuXi AppTec. Purity was confirmed by LC-MS/MS (>98%). The compound was reconstituted with DMSO at 50 mg/ml andwas mixed with cremorphor at 1:1 ratio. Right before use, The C26-A6 stock was diluted with PBS at 1:5 ratio. Mice were injected via tail-vein (T.V.). For the mice that T.V. injection was failed due to the high frequency treatment at late timepoints, i.p. injection with 2x dose was performed instead.

Paclitaxel (Sigma-Aldrich, T7402) stock was prepared at 50mg/ml with ethanol and was diluted with cremorphor with 1:1 ratio. For mouse treatment, ethanol:cremorphor paclitaxel stock was diluted with PBS with 1:5 ratio by vortex right before use (no precipitates were observed).

Statistics and reproducibility

Animals were excluded only if they died or have to be euthanized according to our IACUC protocol. No statistical method was used to predetermine sample size. Data collection and analysis were not performed blinded to the conditions of the experiments. For *in vivo* experiments, animals were randomized and treated as indicated in each experiment. For *in vitro* experiments, all samples were analyzed equally with no sub-sampling; therefore, there was no requirement for randomization. The experiments in Figures 1a, b, h; 2a, f; 3f; 6f; 8g and in Extended Data Figures 1g, m; 2d, g, 3b, e; 6c, g; 7c, d, h; 9c, d, h; 10b, c have been repeated for at least 3 times with similar results. Statistical analyses were indicated in figure captions. Error bars indicate means ± SEM. GraphPad Prism software (version 7) was used for statistical calculations.

Reporting Summary

Further information on research design is available in the Nature Research Reporting Summary linked to this article.

Data availability

All RNA sequencing data generated in this study have been deposited as a superseries at the NCBI Gene Expression Omnibus with the accession code GSE174630. The crystal structure data for SND1/C26-A2 (PDB ID: 7KNW) or A6 (PDB ID: 7KNX) have been deposited at Protein Data Bank. Further information and requests for resources and reagents should be directed to the corresponding author. All requests for raw and analyzed data and materials will be reviewed promptly by the corresponding author to verify whether the request is subject to any intellectual property or confidentiality obligations. Any data and materials that can be shared will be released via a material transfer agreement. Source data supporting the findings of this study are provided with this paper.

Extended Data
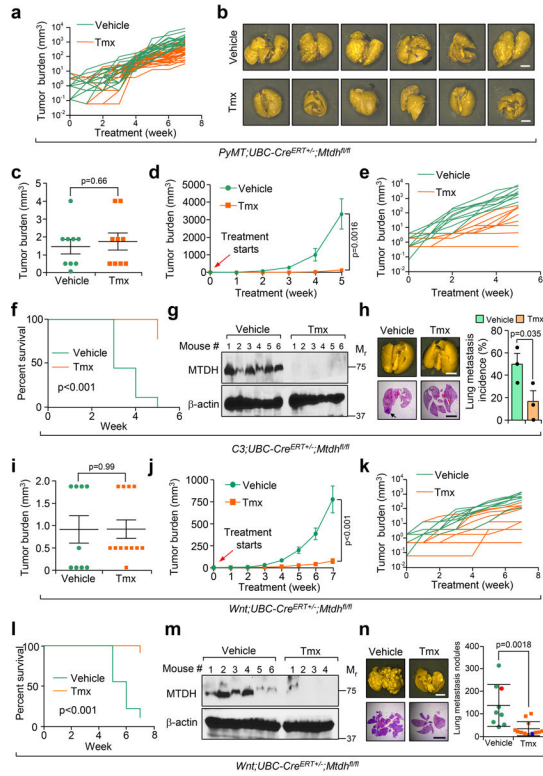
Extended Data Fig. 1. *Mtdh* acute knockout inhibits breast cancer progression and metastasis.
a, Treatment response of each individual mouse in Fig. 1e. **b,** More representative lungs for Fig. 1g. Size bars, 5 mm. **c,i,** Tumor burdens of *FVB.C3;UBC-Cre$^{ERT+/-}$;Mtdh$^{fl/fl}$* (**c**) or *FVB.WNT;UBC-Cre$^{ERT+/-}$;Mtdh$^{fl/fl}$* (**i**) mice before treatment. **d,e and j, k,** Tumor burdens were showed as in groups or individuals in C3 (**d,e**) or WNT (**j,k**) tumor models after treatment. **f,l,** Tumor burden-based survival was plotted. 500 mm^3 was used as cutoff based on the moribund criteria set in our IACUC protocol. p value by Log-rank test. C3 model: Vehicle, n=9; Tmx, n=9 (**c-f**). WNT model: Vehicle, n=9; Tmx, n=12 (**i-l**). **g,m** MTDH expression in tumors from C3 mice (**g**) or WNT mice (**m**) that were treated with vehicle or Tmx was evaluated with western blot. **h,n,** Lungs from C3 mice (**h**) or WNT mice (**n**) were fixed. H&E staining was performed and metastatic incidence (**h**) or nodules were quantified (**n**). The metastatic nodules of the representative lungs were highlighted with red and blue respectively (**n**). C3: Vehicle, n=9 lungs; Tmx, n=9 lung; WNT: Vehicle, n=9 lungs; Tmx, n=12 lung. Size bar, 5 mm (**h,n**). Data represent mean ± SEM. Significance determined by two tailed Student's *t*-test (**c,h,l,n**), two-sided Log-rank test (**f,l**), Two-Way Repeated Measures ANOVA test (**d,j**). Numerical source data for **a, c-f, h-l, n,** and uncropped blots for **g** and **m** are provided.
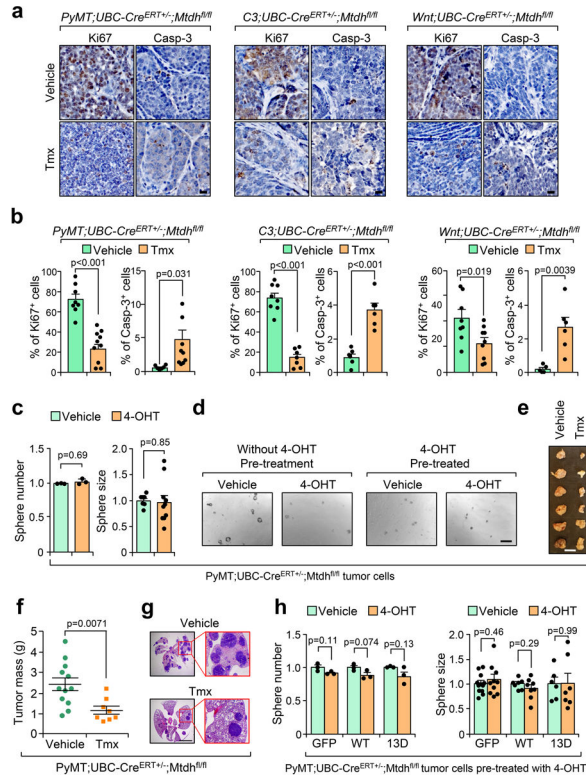
Extended Data Fig. 2. Tamoxifen by itself does not affect tumorsphere formation.
a,b, Primary tumors from PyMT, C3, or WNT mice with vehicle or Tmx treatment were stained with Ki67 or cleaved caspase 3 (Casp-3) (**a**). Images were acquired at non-necrotic/apoptotic areas that were close to tumor border. Positive cells were quantified (**b**). Size bar, 50 μm (**a**). Data represent mean ± SEM. Significance determined by two tailed Student's *t*-test. **c,** *PyMT;UBC-Cre^{ERT+/−};Mtdh^{fl/fl}* cells that were pretreated with 0.02 μg/ml of 4-OHT for 5 days were recovered for another 2 weeks. 25k cells were then seed in each well of the 24-well low attachment plate. One day after seeding, cells were treated with vehicle or 0.02 μg/ml of 4-OHT. 10 days after treatment, sphere number and size were measured and normalized to vehicle control group. Data represent mean ± SEM. n=3 independent experiments. Significance determined by two tailed Student's *t*-test. **d,** Representative images for tumorspheres in Fig. 2b and Extended Data Fig.2c are shown. Size bar, 200 μm. **e,f,** Tumors from Fig. 2d were dissected (**e**) and tumor mass was measured (**f**). Size bar, 2 cm. Data represent mean ± SEM. Significance determined by two tailed Student's *t*-test. **g,** H&E-stained sections of Fig. 2e are complemented by high-magnification images. Size bar, 5 mm. **h,** Cell lines in Fig. 2f were pretreated with 0.02 μg/ml of 4-OHT for 5 days and then recovered for another 2 weeks. The cells were employed for tumorsphere assay with 25k cells per well. Similar treatment as in (**c**) was performed and number and size of the spheres in 4-OHT treatment groups were measured and normalized to vehicle controls of the same cell line. Data represent mean ± SEM. n=3 independent experiments. Significance determined by two tailed Student's *t*-test. Numerical source data for **b, c, f,** and **h** are provided.
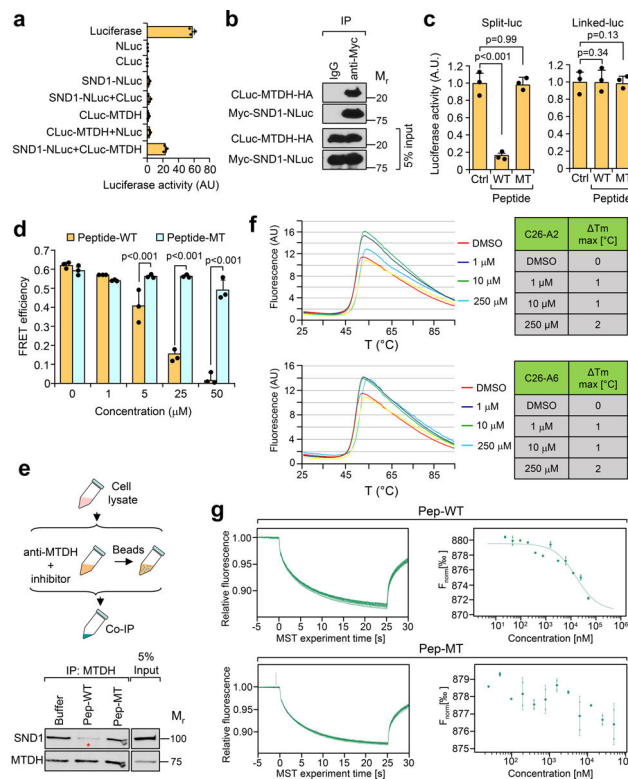
Extended Data Fig. 3. Screening of small chemical compounds that disrupt MTDH/SND1 interaction.

a, 293T cells that expressed wild type luciferase or indicated split-luciferase components were lysed and subjected to luciferase assay. Data represent mean ± SEM. n=3 independent experiments. **b,** 293T cells that were transfected with *CLuc-MTDH-HA* and *Myc-SND1-NLuc* plasmids were lysed for Co-IP assay 3 days later. **c,** 293T cells that express split or linked luciferase components were lysed for luciferase assay. 50 μM of wild type (WT) or SND1 interaction-deficient (MT) MTDH peptides were added into the luciferase assay system. Luciferase activity was measured and normalized to control sample. Data represent mean ± SEM. n=3 independent experiments. Significance determined by one-way ANOVA analysis with Dunnett's test for multiple comparisons. **d,** 0.5 μM of CFP-MTDH and 2 μM of TC-SND1 that labeled with 2.4 μM of FIAsH-EDT$_2$ labeling reagent was used to performed FRET assay in 50 μL system. Indicated concentration of wild type (WT) or mutant (MT) MTDH peptides were added and FRET efficiency was calculated. Data represent mean ± SEM. n=3 independent experiments. Significance determined by one-way ANOVA analysis with Sidak's test for multiple comparisons. **e,** Schematic diagram of Co-IP based confirmation of MTDH-SND1 inhibitory compounds (left). SCP28 cells were lysed for IP assay.2 μg of MTDH antibody together with 500 μM of MTDH wild type (Pep-WT) or mutant (Pep-MT) peptides were added into each 1 ml of samples. Red star indicates wild type MTDH peptide competing off SND1 that binds to MTDH. **f,** 0.1 mg/ml of SND1 purified protein together with the indicated concentration of compounds were applied for thermal melt assay. Melting temperature changes were determined. AU: arbitrary units. **g,** 200 nM of SND1, 50 nM RED-tris-NTA dye and MTDH peptides (24.4 nM-50 μM) were

used to perform Microsacle Thermophoresis (MST) assay. Numerical source data for **a, c, d, f, g** and uncropped blots for **b** and **e** are provided.
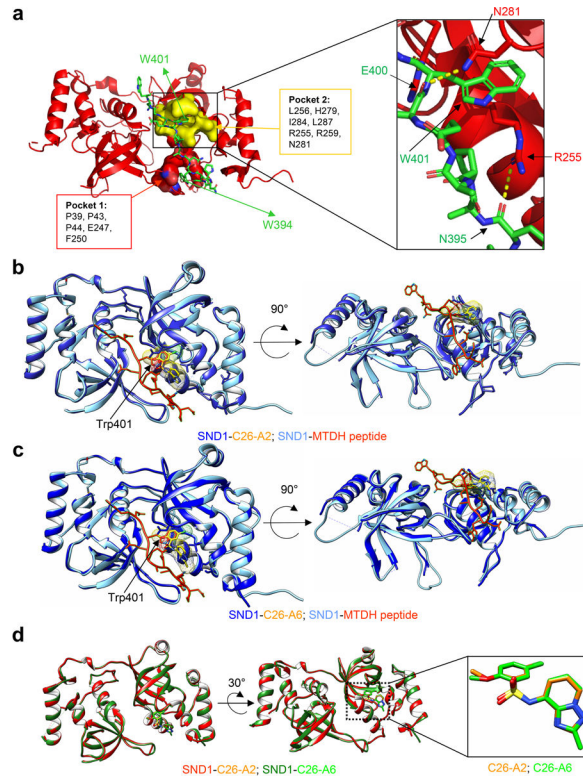
Extended Data Fig. 4. C26-A2 and A6 compete with MTDH to bind the SND1 pocket in the same manner.
a, Overall structures of MTDH-SND1 complex (top). A close-up view is shown at SND1 pocket 2 (bottom). SND1 is shown in red ribbon and cylinder (side chain). MTDH is shown in worm (backbone) and cylinder (side chain) and colored green. **b,c,** Overall structures of SND1-C26-A2 and SND1-MTDH complexes (**b**) or SND1-C26-A6 and SND1-MTDH complexes (**c**). Two perpendicular views are shown. In SND1-C26-A2 and SND1-C26-A6, SND1 is shown in dark blue ribbon, C26-A2 and A6 are shown in orange backbone and surface; In SND1-MTDH complex, SND1 is shown in light blue ribbon, and MTDH is shown in worm (backbone) and cylinder (side chain) and colored red. **d,** Overall structures of SND1-C26-A2 and SND1-C26-A6 complexes (left). Two perpendicular views are shown. A close-up view of C26-A2 and A6 is shown at SND1 pocket (Right). In SND1-C26-A2, SND1 is shown in red ribbon, C26-A2 is shown in orange backbone; In SND1-C26-A6, SND1 is shown in dark green ribbon, C26-A6 is shown in green backbone.

a

Compounds	Direction	Recovery (%)	$P_{app}(10^{-6}$cm/s)			Efflux ratio	Absorption potential classification	Significant efflux
			R1	R2	AVE			
C26-A2	A-to-B	94	74.8	71.8	73.3	1.5	High	No
	B-to-A	95	116	106	111			
C26-A6	A-to-B	86	52.3	46.6	49.4	1	High	No
	B-to-A	86	53.4	43.3	48.4			
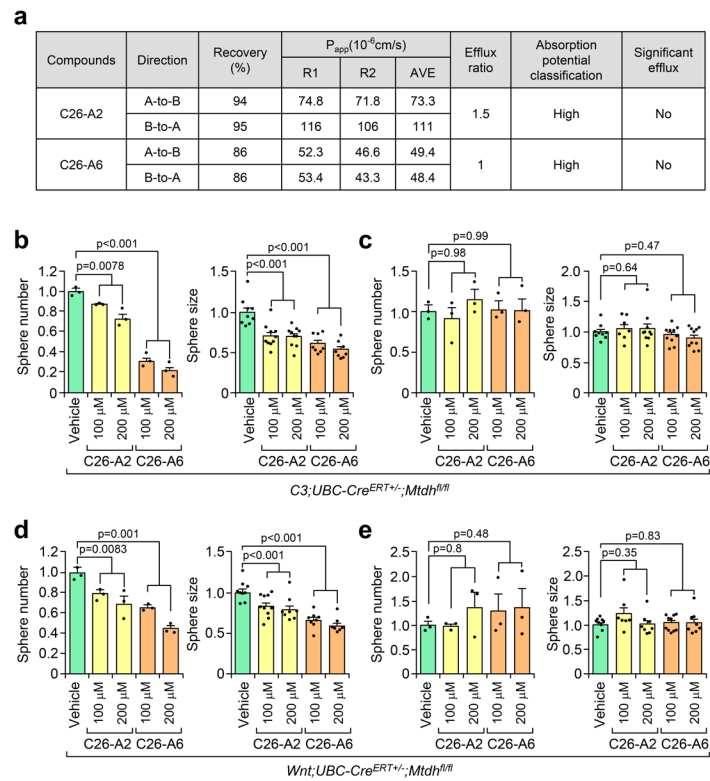
Extended Data Fig. 5. C26-A2 and A6 inhibits tumorsphere formation *in vitro*.
a, Caco-2 cells were employed to test cell permeability of C26-A2 and A6. 5 μM of compounds were dosed on both apical side (A-to-B) and basolateral side (B-to-A). Samples were taken from the donor and receiver chambers at 120 min after treatment. All samples were assayed by LC-MS/MS using electrospray ionization. The apparent permeability (P_{app}) and percent recovery were calculated. **b-e,** *C3;UBC-Cre^ERT+/−^;Mtdh^fl/fl^* (**b,c**) and *Wnt;UBC-Cre^ERT+/−^;Mtdh^fl/fl^* tumor cells (**d,e**) that with (**c,e**) or without (**b,d**) 5 days of 0.02 μg/ml 4-OHT pre-treatment were subjected to the tumorsphere assay. 50k per well of cells were seed and treated with indicated compounds the next day. 5 days after treatment, sphere number and size were assessed and normalized to vehicle control group. Data represent mean ± SEM. n=3 independent experiments. Significance determined by one-way ANOVA analysis with Dunnett's test for multiple comparisons. Numerical source data for **b-e** are provided.
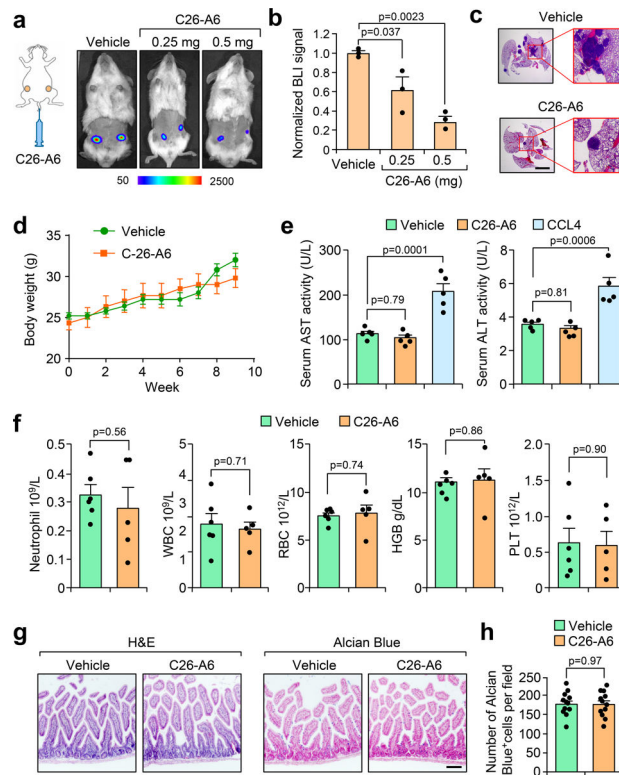
Extended Data Fig. 6. C26-A6 treatment blocks MTDH/SND1 interaction *in vivo* with limited toxicity.

a,b, NSG female mice were inoculated with 10k of SCP28 cells that express split-luciferase components by MFP injection. Two weeks after injection, the mice were treated with 0.25 mg/mouse or 0.5 mg/mouse of C26-A6 via tail-vein injection. 30 min after the treatment, luciferase activity at primary tumors was measured. Data represent mean ± SEM. n=3 mice. Significance determined by one-way ANOVA analysis with Dunnett's test for multiple comparisons. **c,** H&E-stained sections of Fig. 6d are complemented by high-magnification images. Size bar, 5 mm. **d,** Body weight of the mice in experiment Fig. 6b was measured. Vehicle, n=10 mice; C26-A6, n=12 mice. **e,** Serum from mice in experiment in Fig. 6b were collected for ALT and AST activity measurement following the standard protocol (Sigma). Three FVB females treated with 200 μl of 8% CCl4 in corn oil for 2 days served as positive control. Data represent mean ± SEM. n=5 mice per group. Significance determined by one-way ANOVA analysis with Dunnett's test for multiple comparisons. **f,** Blood samples were drawn from the heart of mice in experiment Fig. 6b, and blood cell counts were performed with the Sysemx XN-3000 Hematology System (Sysmex America, Inc.) Data represent mean ± SEM. Vehicle, n=6 mice; C26-A6, n=5 mice. Significance determined by two tailed Student's *t*-test**. g,** Small intestine samples were obtained from mice in experiment Fig. 6b. H&E and Alcian blue staining was performed on processed, sliced samples. Scale bar: 200 μm. **h,** Quantification of Alcian blue staining results from (**g**). Data represent mean ± SEM. n=12 fields from 5 mice in each group. Significance determined by two tailed Student's *t*-test. Numerical source data for **b, d-f,** and **h** are provided.
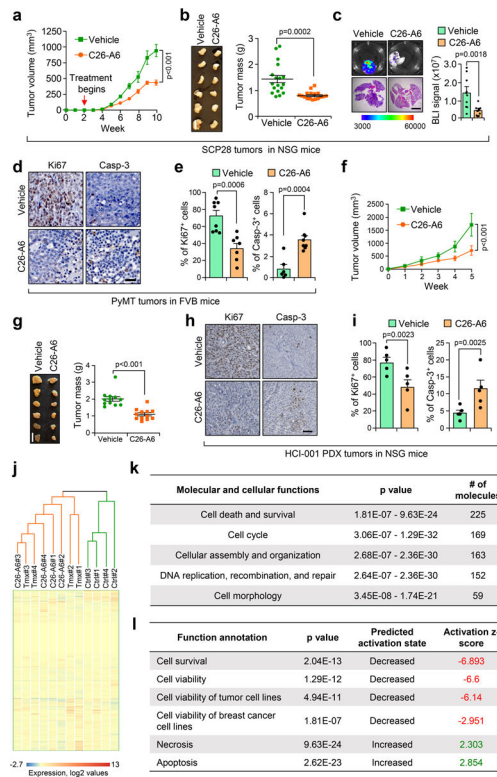
Extended Data Fig. 7. C26-A6 inhibits breast cancer progression and metastasis.
a-c, NGS female mice injected with 2k SCP28 cells orthotopically were subjected to vehicle or C26-A6 treatment after two weeks. Primary tumor volumes were measured(**a**). 8 weeks after treatment, tumor mass (**b**) and lung metastasis (**c**) were assessed. Vehicle, n= 10 mice; C26-A6, n=10 mice. Size bars, 2 cm for (**b**) and 5 mm for (**c**). **d,e,** Primary tumors from experiment in Fig. 6b were stained with Ki67 and Cleaved-Caspase 3 (Casp-3) antibodies (**d**). Positive cells were quantified (**e**). Size bar, 100 μm. Data represent mean ± SEM. n=6 mice. **f,** Fresh HCI-001 PDX tumors were implanted into the mammary glands of female NSG mice. One day after implantation, the mice were treated with vehicle or C26-A6. Primary tumors were monitored. **g,** Primary tumors from (**f**) were weighted. Representative tumors are shown. Size bar, 2 cm. n=12 tumors per group. **h,i,** Primary tumors from (**f**) were stained with Ki67 and cleaved-Caspase 3 (Casp-3) antibodies (**h**). Positive cells were quantified (**i**). Size bar, 200 μm. n=5 tumors per group. **j,** Heatmap representation of Next-generation sequencing data displaying the expression of genes in tumors that treated with vehicle (Ctrl), 60 mg/kg of Tmx for 5 consecutive days, or 15 mg/kg of C26-A6 5 days per week. Color key indicates log2 values. n=4 mice per group. **k,l,** Ingenuity pathway analysis shows the top five molecular and cellular functions of C26-A6 treatment-downregulated genes (n=620, fold change >2, p < 0.05) (**k**). Effects of C26-A6 treatment-downregulated genes in cell death and survival functions (**l**). p values were automatically determined by QIAGEN Ingenuity Pathway Analysis (QIAGEN IPA). Data represent mean ± SEM. Significance determined by Two-Way Repeated Measures ANOVA test (**a,f**) and two tailed Student's *t*-test (**b,c,e,g,i**). Numerical source data for **a-c, e, f, g,** and **i** are provided.
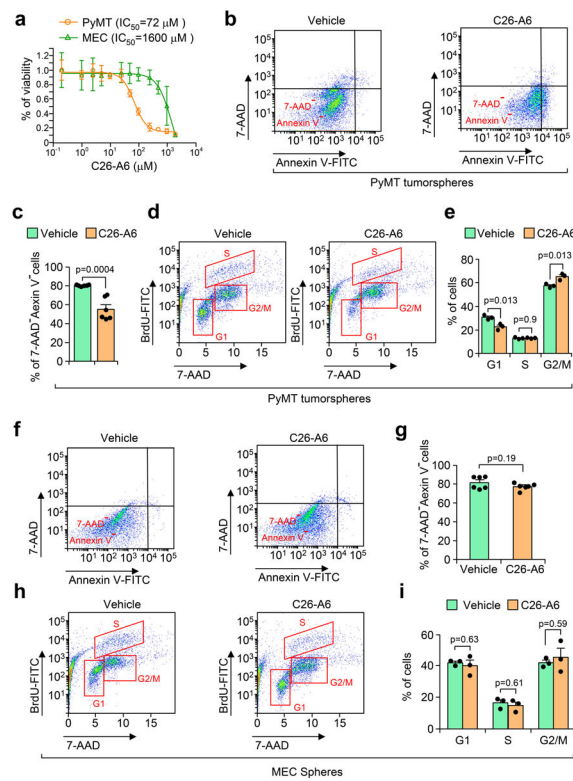
Extended Data Fig. 8. C26-A6 induces cell cycle arrest and reduces cell viability.
a, Spheres were treated with vehicle or indicated concentrations of C26-A6 for 1 week. The viability of the spheres was then quantified by MTT assay. **b-i,** Similar sphere assay as in (**a**) was performed. The apoptosis (**b,f**) and cell cycle status (**d,h**) were determined. The live cells (**c,g**) and percentage of the cells in each cell cycle phase (**e,i**) were quantified. n 3 independent experiments. Data represent mean ± SEM and significance determined by two tailed Student's *t*-test for all panels. Numerical source data for **a, c, e, g,** and **i** are provided.
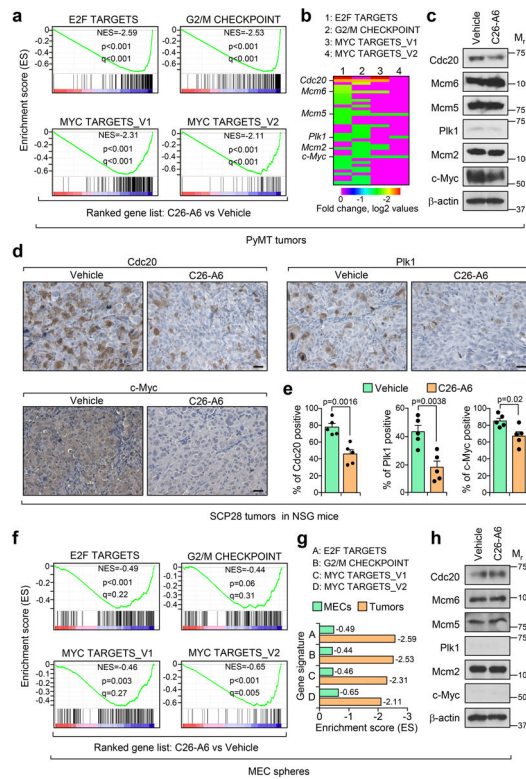
Extended Data Fig. 9. Pathways that are altered upon C26-A6 treatment.
a, Gene set enrichment analysis plot showing the top 4 gene signatures in ranked list of genes. **b,** Leading edge analysis was performed with the 4 gene signature and the heatmap of top candidate genes was shown. Color key indicates log2 values. **c,** Sphere assay was performed and treated with vehicle and C26-A6 as in Extended Data Fig. 8a. The spheres were collected for western blot to analyze the expression of the candidates. **d,e,** Primary tumors from experiment in Extended Data Fig. 7a were stained with indicated antibodies (**d**). Positive cells were quantified (**e**). Size bars, 50 μm. n=5 tumors per group. Data represent mean ± SEM and significance determined by two tailed Student's *t*-test (**e**). **f-h,** Mammary epithelial cell (MEC) spheres were treated with vehicle or C26-A6 for 1 week. The spheres were then harvested for RNA-sequencing and followed by gene set enrichment analysis(**f**). The normalized enrichment scores of the indicated signatures in C26-A6 treated MECs and tumors are shown (**g**). MEC spheres in (**f**) were collected for western blot analysis with indicated antibodies. Numerical source data for **e** and uncropped blots for **c** and **h** are provided.

Extended Data Fig. 10. C26-A6 inhibits metastatic breast cancer progression.
a, Indicated cells were injected into NSG females orthotopically and followed by vehicle or C26-A6 treatment after 2 weeks. Tumor volumes were measured 8 weeks after injection. Vehicle, n=6 mice; C26-A6, n=6 mice. **b,** Spontaneous lung metastasis of the mice in (**a**) were assessed by BLI (right). Size bar, 5 mm. Vehicle, n=5 lungs; C26-A6, n=6 lungs. **c,** The SND1 and MTDH expression of the cells used in (**a**) was evaluated. **d,e,** Tail-vein injection lung metastasis was determined by BLI right before (Week 0) or after (5 weeks) vehicle or C26-A6 treatment (**f**).. Lung metastatic nodules were quantified. The metastatic nodules of the representative lungs were highlighted with red and blue respectively. Size bar, 5 mm (**e**). Vehicle, n=11 lungs; C26-A6, n=12 lungs. **f,g,** SUM159-M1a cells were injected into NSG females orthotopically. 2 weeks after injection, the mice were treated with vehicle or C26-A6. 5 weeks later, primary tumors (**f**) and spontaneous lung metastasis (**g**) were measured. n=10 mice per group. **h,i,** Tail-vein injection lung metastasis was determined by BLI right before (Week 0) or after (5 weeks) vehicle or C26-A6 treatment (**h**).The metastatic nodules of the representative lungs were highlighted with red and blue respectively (**i**). n=12 mice per group. Size bar, 5 mm. **j,k,** 4T1 cells were injected into Balb/C females orthotopically. 1 week after injection, the mice were treated with vehicle or C26-A6. 5 weeks after the treatment, primary tumors (**j**) and spontaneous lung metastasis (**k**) were measured. n=10 mice per group. **l,** 4T1 cells were injected into Balb/C females intravenously. 5 weeks after vehicle or C26-A6 treatment, lung metastatic nodules were counted. The metastatic nodules of the representative lungs were highlighted with red and blue respectively. Vehicle, n=5 mice; C26-A6, n=6 mice. Size bar, 5 mm. Data represent

mean ± SEM andsignificance determined by two tailed Student's *t*-test for all panels. Numerical source data for **a, b, d-l** and uncropped blots for **c** are provided.

Supplementary Material

Refer to Web version on PubMed Central for supplementary material.

Acknowledgements

References

1. Nguyen DX, Bos PD & Massague J Metastasis: from dissemination to organ-specific colonization. Nature reviews 9, 274–284 (2009).

2. Hu G, Wei Y & Kang Y The multifaceted role of MTDH/AEG-1 in cancer progression. Clin Cancer Res 15, 5615–5620 (2009). [PubMed: 19723648]

3. Wan L & Kang Y Pleiotropic roles of AEG-1/MTDH/LYRIC in breast cancer. Advances in cancer research 120, 113–134 (2013). [PubMed: 23889989]

4. Wan L et al. MTDH-SND1 interaction is crucial for expansion and activity of tumor-initiating cells in diverse oncogene- and carcinogen-induced mammary tumors. Cancer cell 26, 92–105 (2014). [PubMed: 24981741]

5. Wan L et al. Genetic ablation of metadherin inhibits autochthonous prostate cancer progression and metastasis. Cancer research 74, 5336–5347, doi:10.1158/0008-5472.CAN-14-1349 (2014). [PubMed: 25074613]

6. Jariwala N et al. Role of the staphylococcal nuclease and tudor domain containing 1 in oncogenesis (review). International journal of oncology 46, 465–473 (2014). [PubMed: 25405367]

7. Shen M et al. Therapeutic Targeting of Metadherin Suppresses Colorectal and Lung Cancer Progression and Metastasis. Cancer research 81, 1014–1025, doi:10.1158/0008-5472.CAN-20-1876 (2021). [PubMed: 33239430]

8. Blanco MA et al. Identification of staphylococcal nuclease domain-containing 1 (SND1) as a Metadherin-interacting protein with metastasis-promoting functions. The Journal of biological chemistry 286, 19982–19992 (2011). [PubMed: 21478147]

9. Yoo BK et al. Increased RNA-induced silencing complex (RISC) activity contributes to hepatocellular carcinoma. Hepatology 53, 1538–1548, doi:10.1002/hep.24216 (2011). [PubMed: 21520169]

10. Jariwala N et al. Role of the staphylococcal nuclease and tudor domain containing 1 in oncogenesis (review). International journal of oncology 46, 465–473, doi:10.3892/ijo.2014.2766 (2015). [PubMed: 25405367]

11. Van Nostrand EL et al. A large-scale binding and functional map of human RNA-binding proteins. Nature 583, 711–719, doi:10.1038/s41586-020-2077-3 (2020). [PubMed: 32728246]

12. Guo F et al. Structural insights into the tumor-promoting function of the MTDH-SND1 complex. Cell reports 8, 1704–1713 (2014). [PubMed: 25242325]

13. Du J et al. PDK1 promotes tumor growth and metastasis in a spontaneous breast cancer model. Oncogene 35, 3314–3323, doi:10.1038/onc.2015.393 (2016). [PubMed: 26455327]

14. Canovas B et al. Targeting p38alpha Increases DNA Damage, Chromosome Instability, and the Anti-tumoral Response to Taxanes in Breast Cancer Cells. Cancer cell 33, 1094–1110 e1098, doi:10.1016/j.ccell.2018.04.010 (2018). [PubMed: 29805078]

15. Klein A et al. Comparison of gene expression data from human and mouse breast cancers: identification of a conserved breast tumor gene set. International journal of cancer 121, 683–688 (2007). [PubMed: 17410534]

16. Kretschmer C et al. Identification of early molecular markers for breast cancer. Molecular cancer 10, 15 (2011). [PubMed: 21314937]

17. Maroulakou IG, Anver M, Garrett L & Green JE Prostate and mammary adenocarcinoma in transgenic mice carrying a rat C3(1) simian virus 40 large tumor antigen fusion gene. Proceedings of the National Academy of Sciences of the United States of America 91, 11236–11240 (1994). [PubMed: 7972041]

18. Cho RW et al. Isolation and molecular characterization of cancer stem cells in MMTV-Wnt-1 murine breast tumors. Stem cells (Dayton, Ohio) 26, 364–371 (2008).

19. Hollern DP & Andrechek ER A genomic analysis of mouse models of breast cancer reveals molecular features of mouse models and relationships to human breast cancer. Breast Cancer Res 16, R59 (2014). [PubMed: 25069779]

20. Pond AC et al. Fibroblast growth factor receptor signaling dramatically accelerates tumorigenesis and enhances oncoprotein translation in the mouse mammary tumor virus-Wnt-1 mouse model of breast cancer. Cancer research 70, 4868–4879 (2010). [PubMed: 20501844]

21. Luker KE et al. Kinetics of regulated protein-protein interactions revealed with firefly luciferase complementation imaging in cells and living animals. Proceedings of the National Academy of Sciences of the United States of America 101, 12288–12293 (2004). [PubMed: 15284440]

22. Paulmurugan R & Gambhir SS Combinatorial library screening for developing an improved split-firefly luciferase fragment-assisted complementation system for studying protein-protein interactions. Analytical chemistry 79, 2346–2353 (2007). [PubMed: 17295448]

23. Porter JR, Stains CI, Jester BW & Ghosh I A general and rapid cell-free approach for the interrogation of protein-protein, protein-DNA, and protein-RNA interactions and their antagonists utilizing split-protein reporters. Journal of the American Chemical Society 130, 6488–6497 (2008). [PubMed: 18444624]

24. Hoffmann C et al. A FlAsH-based FRET approach to determine G protein-coupled receptor activation in living cells. Nature methods 2, 171–176 (2005). [PubMed: 15782185]

25. Kang Y et al. A multigenic program mediating breast cancer metastasis to bone. Cancer cell 3, 537–549 (2003). [PubMed: 12842083]

26. Groftehauge MK, Hajizadeh NR, Swann MJ & Pohl E Protein-ligand interactions investigated by thermal shift assays (TSA) and dual polarization interferometry (DPI). Acta crystallographica 71, 36–44 (2015).

27. Jerabek-Willemsen M, Wienken CJ, Braun D, Baaske P & Duhr S Molecular interaction studies using microscale thermophoresis. Assay and drug development technologies 9, 342–353 (2011). [PubMed: 21812660]

28. Wienken CJ, Baaske P, Rothbauer U, Braun D & Duhr S Protein-binding assays in biological liquids using microscale thermophoresis. Nature communications 1, 100 (2010).

29. van Breemen RB & Li Y Caco-2 cell permeability assays to measure drug absorption. Expert opinion on drug metabolism & toxicology 1, 175–185 (2005). [PubMed: 16922635]

30. DeRose YS et al. Tumor grafts derived from women with breast cancer authentically reflect tumor pathology, growth, metastasis and disease outcomes. Nat Med 17, 1514–1520, doi:10.1038/nm.2454 (2011). [PubMed: 22019887]

31. Esposito M et al. Bone vascular niche E-selectin induces mesenchymal-epithelial transition and Wnt activation in cancer cells to promote bone metastasis. Nature cell biology 21, 627–639 (2019). [PubMed: 30988423]

32. Shen M et al. Tinagl1 Suppresses Triple-Negative Breast Cancer Progression and Metastasis by Simultaneously Inhibiting Integrin/FAK and EGFR Signaling. Cancer cell 35, 64–80 e67 (2019). [PubMed: 30612941]

33. Kaur P et al. A mouse model for triple-negative breast cancer tumor-initiating cells (TNBC-TICs) exhibits similar aggressive phenotype to the human disease. BMC Cancer 12, 120, doi:10.1186/1471-2407-12-120 (2012). [PubMed: 22452810]

34. Arkin MR, Tang Y & Wells JA Small-molecule inhibitors of protein-protein interactions: progressing toward the reality. Chemistry & biology 21, 1102–1114 (2014). [PubMed: 25237857]

35. Lage K Protein-protein interactions and genetic diseases: The interactome. Biochimica et biophysica acta 1842, 1971–1980 (2015).

36. Scott DE, Bayly AR, Abell C & Skidmore J Small molecules, big targets: drug discovery faces the protein-protein interaction challenge. Nature reviews 15, 533–550 (2016).

37. Jubb H, Higueruelo AP, Winter A & Blundell TL Structural biology and drug discovery for protein-protein interactions. Trends in pharmacological sciences 33, 241–248 (2012). [PubMed: 22503442]

38. Surade S & Blundell TL Structural biology and drug discovery of difficult targets: the limits of ligandability. Chemistry & biology 19, 42–50 (2012). [PubMed: 22284353]

39. Tari LW The utility of structural biology in drug discovery. Methods in molecular biology (Clifton, N.J 841, 1–27 (2012).

40. Jin L, Wang W & Fang G Targeting protein-protein interaction by small molecules. Annual review of pharmacology and toxicology 54, 435–456 (2013).

41. Nero TL, Morton CJ, Holien JK, Wielens J & Parker MW Oncogenic protein interfaces: small molecules, big challenges. Nat Rev Cancer 14, 248–262 (2014). [PubMed: 24622521]

42. Vassilev LT et al. In vivo activation of the p53 pathway by small-molecule antagonists of MDM2. Science (New York, N.Y 303, 844–848 (2004).

43. Zhao J et al. Discovery and structural characterization of a small molecule 14–3-3 protein-protein interaction inhibitor. Proceedings of the National Academy of Sciences of the United States of America 108, 16212–16216 (2011). [PubMed: 21908710]

44. Zimmermann G et al. Small molecule inhibition of the KRAS-PDEdelta interaction impairs oncogenic KRAS signalling. Nature 497, 638–642 (2013). [PubMed: 23698361]

45. Jiang YZ et al. Preoperative measurement of breast cancer overestimates tumor size compared to pathological measurement. PLoS One 9, e86676, doi:10.1371/journal.pone.0086676 (2014). [PubMed: 24489766]

46. Jiang YZ et al. Transcriptome Analysis of Triple-Negative Breast Cancer Reveals an Integrated mRNA-lncRNA Signature with Predictive and Prognostic Value. Cancer research 76, 2105–2114 (2016). [PubMed: 26921339]

47. Liu YR et al. Comprehensive transcriptome analysis identifies novel molecular subtypes and subtype-specific RNAs of triple-negative breast cancer. Breast Cancer Res 18, 33 (2016). [PubMed: 26975198]

48. Subramanian A et al. Gene set enrichment analysis: a knowledge-based approach for interpreting genome-wide expression profiles. Proceedings of the National Academy of Sciences of the United States of America 102, 15545–15550 (2005). [PubMed: 16199517]

49. Mootha VK et al. PGC-1alpha-responsive genes involved in oxidative phosphorylation are coordinately downregulated in human diabetes. Nature genetics 34, 267–273 (2003). [PubMed: 12808457]

50. Kozlov AG, Galletto R & Lohman TM SSB-DNA binding monitored by fluorescence intensity and anisotropy. Methods in molecular biology (Clifton, N.J 922, 55–83, doi:10.1007/978-1-62703-032-8_4 (2012).

51. Okoye-Okafor UC et al. New IDH1 mutant inhibitors for treatment of acute myeloid leukemia. Nat Chem Biol 11, 878–886, doi:10.1038/nchembio.1930 (2015). [PubMed: 26436839]
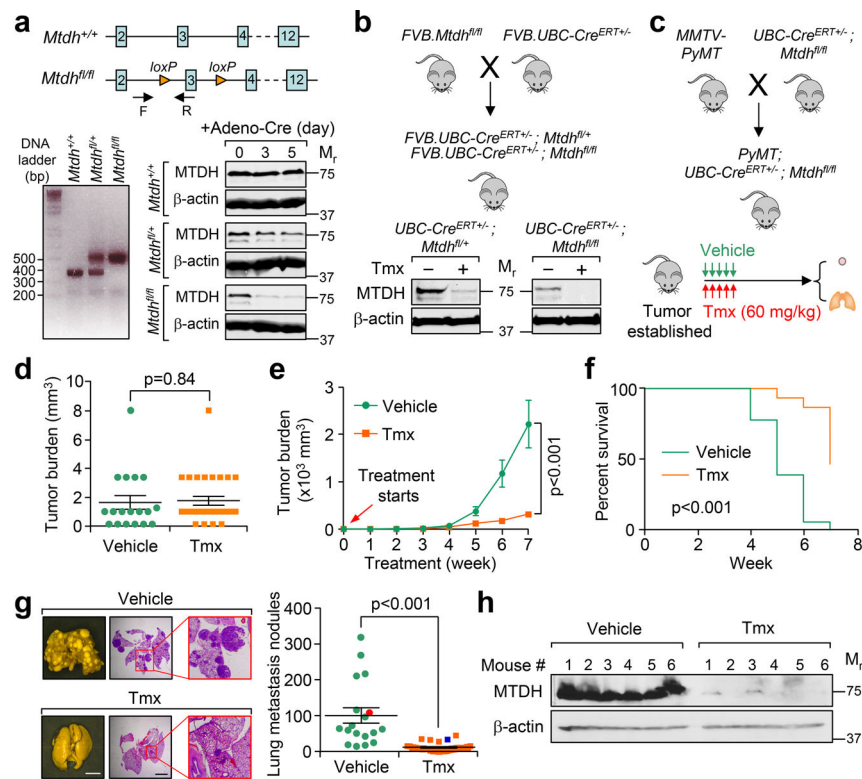
Fig. 1. Induced *Mtdh* knockout suppresses breast cancer progression and metastasis.

a, Schematic diagram of *Mtdh^floxed/floxed^* (*Mtdh^fl/fl^*) mice (Top). Genotyping result of *Mtdh* wild type (*Mtdh^+/+^*, 371bp), conditional *Mtdh* knockout heterozygous (*Mtdh^fl/+^*, 371bp and 522bp), and conditional *Mtdh* knockout homozygous (*Mtdh^fl/fl^*, 522bp) (bottom left). Western blotting of MTDH in splenocytes from indicated strains cultured with multiplicity of infection (MOI, 100) adenovirus expressing Cre for 0, 3, or 5 days (bottom right). F, forward primer and R, reverse primer for genotyping. **b,** Schematic diagram of generation of *Mtdh* inducible knockout mice (Top). Cre expression is induced by Tamoxifen (Tmx) in *FVB. UBC-Cre^ERT+/−^* strain. **c,** *FVB.UBC-Cre^ERT+/−^;Mtdh^fl/fl^* strain was breed with *FVB.MMTV-PyMT* strain to generate breast cancer mouse model with *Mtdh* inducible knockout. Mice with matched tumor sizes were treated with Tmx or vehicle for 5 consecutive days via i.p. Tumors were measured weekly and lung metastasis was evaluated at endpoint. **d,** *FVB.PyMT;UBC-Cre^ERT+/−^; Mtdh^fl/fl^* mice with tumors established were split into two groups with matched tumor sizes for vehicle (n=18 mice) or Tmx (n=30 mice) treatment respectively. Tumor burden before treatment was showed. Data represent mean ± SEM. Significance determined by two tailed Student's *t*-test**. e,** Tumor progression curves are shown after treatment starts. Each primary tumor is measured, and sizes were added as tumor burden in each mouse after treatment. Vehicle, n=18; Tmx, n=30. Data represent mean ± SEM. Significance determined by Two-Way Repeated Measures ANOVA test. **f,** Tumor burden-based survival was plotted. 500 mm^3 was used as cutoff for moribund condition as defined in the IACUC protocol. p value by two-sided Log-rank test. Vehicle, n=18; Tmx, n=30. **g,** Lungs were collected, fixed and subjected to H&E staining (Left). Metastatic nodules were counted (right). The metastatic nodules of the representative lungs were highlighted with red and blue respectively (right). Vehicle, lung=18; Tmx, lung=30.

Size bar, 5 mm. Data represent mean ± SEM. Significance determined by two tailed Student's *t*-test. **h,** MTDH expression in tumors from the mice treated with vehicle or Tmx was evaluated with western blot. Numerical source data for **d, e, f, g,** and uncropped blots for **h** are provided.
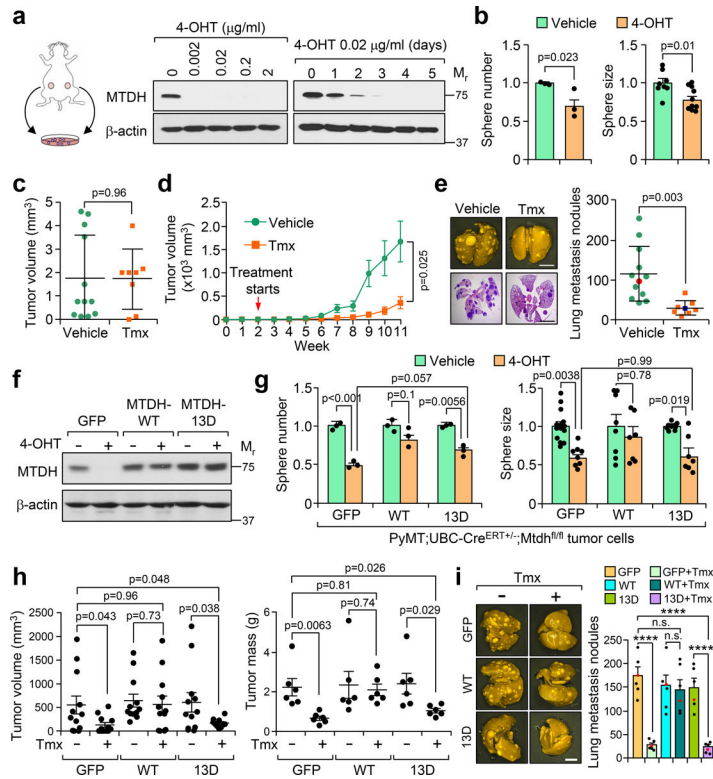
Fig. 2. MTDH-SND1 interaction is essential for breast cancer progression and metastasis.
a, Primary tumors from *FVB.PyMT;UBC-Cre^{ERT+/−};Mtdh^{fl/fl}* mice were cultured to generate cell line (left). The cell line that treated with 4-OHT were harvested for western blotting (right). 4-OHT, (Z)-4-Hydroxytamoxifen. **b,** Tumorsphere assay was performed with *FVB.PyMT; UBC-Cre^{ERT+/−};Mtdh^{fl/fl}* cells. Sphere number and size were determined and normalized to vehicle group. Data represent mean ± SEM. n=3 independent experiments. Significance determined by two tailed Student's *t*-test. **c,d,** 10k of *FVB.PyMT; UBC-Cre^{ERT+/−};Mtdh^{fl/fl}* cells were orthotopically inoculated into FVB females. Two weeks after injection, mice were treated with or without Tmx. Tumors were measured before (**c**) and after treatment (**d**). Vehicle, n=12, Tmx, n=8. Data represent mean ± SEM. Significance determined by two tailed Student's *t*-test (**c**) and Two-Way Repeated Measures ANOVA test (**d**). **e,** 11 weeks after injection, lungs were collected, and metastatic nodules were counted. The metastatic nodules of the representative lungs were highlighted with red and blue respectively. Size bar, 5 mm. Vehicle, lung=12; Tmx, lung=8. Data represent mean ± SEM. Significance determined by two tailed Student's *t*-test. **f,** *PyMT;UBC-Cre^{ERT+/−};Mtdh^{fl/fl}* cells with GFP (vector), wild type MTDH (MTDH-WT), or SND1 interaction deficient MTDH (MTDH-13D) expressing were treated with4-OHT followed by western blotting. **g,** Sphere number and size in 4-OHT treatment groups were determined and normalized to vehicle controls of the same cell line. Data represent mean ± SEM. n=3 independent experiments. Significance determined by one-way ANOVA analysis with Sidak's test for multiple comparisons. **h,** 50k of the indicated cells were orthotopically injected into FVB female mice. One week after injection, the mice were treated with or without Tmx. 6 weeks later, tumor size and weight were measured. n=6 mice per group. Data represent mean

± SEM. Significance determined by two tailed Student's *t*-test. **i,** Lungs were fixed, and the metastatic nodules were quantified. The metastatic nodules of the representative lungs were highlighted with red. n=6 lungs per group. Size bar, 5mm. Data represent mean ± SEM. Significance determined by two tailed Student's *t*-test. (n.s. p>0.05, ****p<0.0001.) Numerical source data for **b-e, g-i,** and uncropped blots for **a** and **f** are provided.
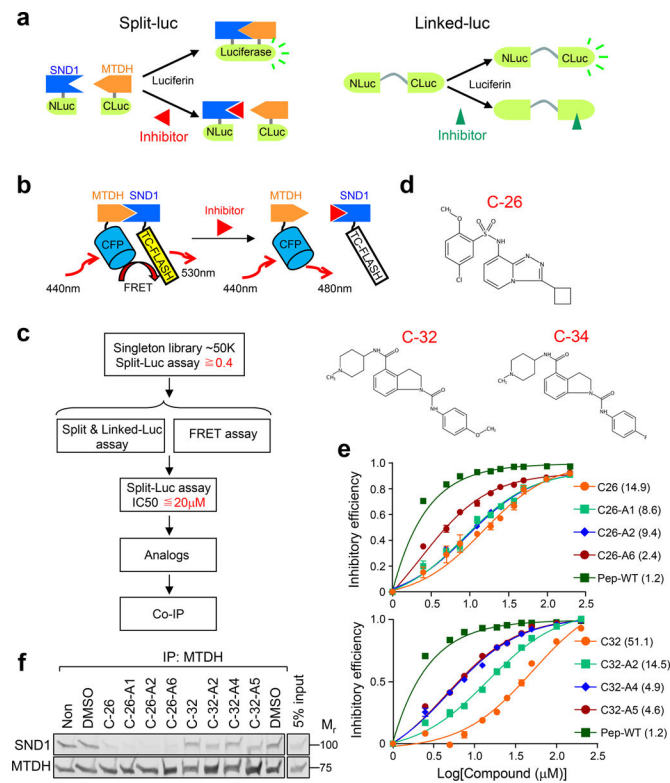
Fig. 3. Identification of small chemical inhibitors that block MTDH-SND1 interaction.
a,b, Schematic diagrams of the small molecule screening platforms. Split & Linked-luciferase (Split-luc, Linked-luc) assay (**a**) and FRET assay (**b**). **c,** Workflow of the screening. **d,** Structure of the three positive candidates. **e,** Split-luciferase assay was performed with multiple doses of indicated compounds or MTDH wild type peptide (Pep-WT). Data represent mean ± SEM. Luciferase inhibitory efficiency was calculated, and curves were fit. IC50s (μM) are shown following each compound/peptide. **f,** SCP28 cells grow confluent in each 10 cm dish were lysed with 1 ml of IP lysis buffer. 500 μM of the compounds were added into each 1 ml of the samples and IP with 2 μg of anti-MTDH antibody. Western blot was then performed to detect SND1 that binds to MTDH. Numerical source data for **e,** and uncropped blots for **f** are provided.
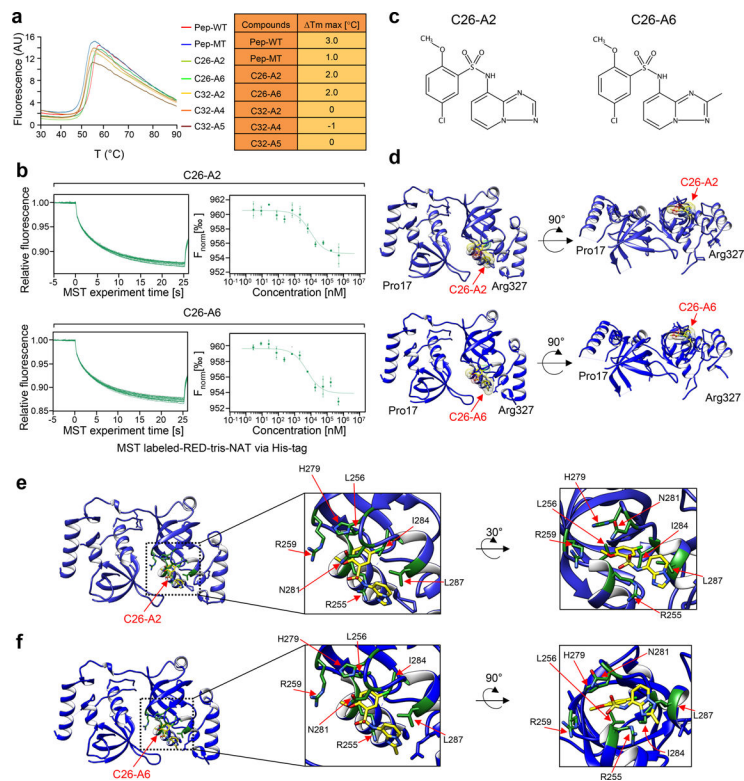
Fig. 4. C26s block MTDH binding pocket on SND1 to disrupt MTDH-SND1 complex.
a, 0.1 mg/ml of SND1 purified protein together with 250 μM of MTDH peptides or indicated compounds were applied for thermal melt assay. Melting temperature changes were determined. **b,** 150 nM of SND1, 50 nM RED-tris-NTA dye and compounds (2.82 nM-500 μM) were used to perform Microscale Thermophoresis (MST) assay. **c,** Structure of compounds C26-A2 and A6. **d,** Overall structures of SND1-C26-A2 (top) and SND1-C26-A6 (bottom) complex. Two perpendicular views are shown. SND1 is shown in blue ribbon. C26-A2 and A6 are shown in backbone and surface. C26-A2 and A6 are indicated with red arrows. **e,f,** Close-up views of SND1-C26-A2 (**e**) and SND1-C26-A6 (**f**) complexes. Two perpendicular views are shown. SND1 is shown in ribbon (blue) and cylinder (indicated residues, green). C26-A2 and A6 are shown in backbone (yellow). Numerical source data for **a** and **b** are provided.
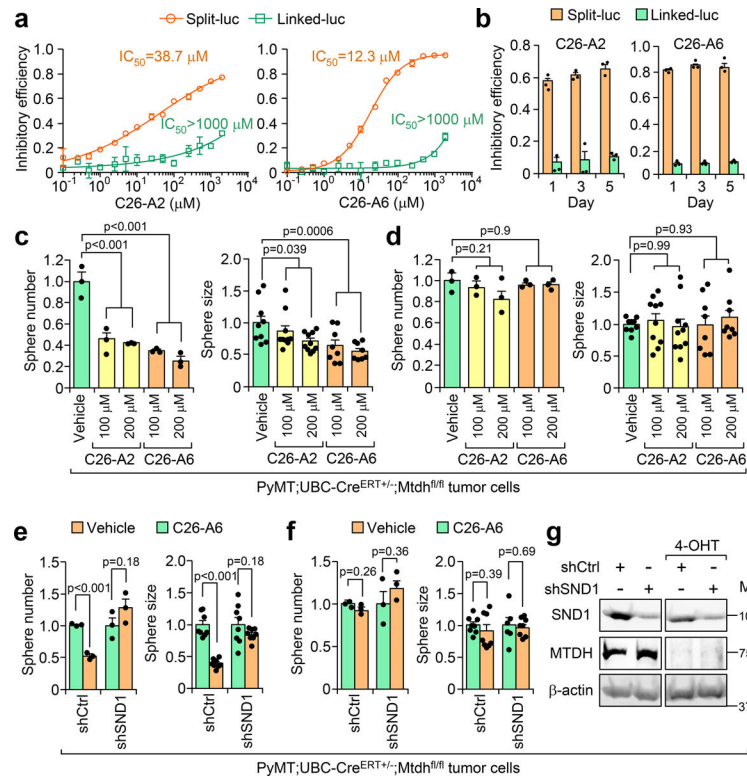
Fig. 5. C26-A2 and A6 suppress tumor formation *in vitro*.

a, SCP28 cells that stably express split- or linked-luciferase components were treated with multiple doses of C26-A2 or C26-A6. 30 min after treatment, culture media was removed and the luciferase activity in the cells was measured. Data represent mean ± SEM. n=3 independent experiments. **b,** The same cells in (**a**) that treated with 100 μM of the compounds for indicated days were harvested to measure the luciferase activity. Data represent mean ± SEM. n=3 independent experiments. **c,d,** *PyMT;UBC-Cre^{ERT+/−};Mtdh^{fl/fl}* cells with (**d**) or without (**c**) 5 days of 0.02 μg/ml 4-OHT pre-treatment was employed for tumorsphere assay. 50k per well of cells were seed and treated with indicated compounds the next day. 5 days after treatment, sphere number and size were assessed and normalized to vehicle control group. Data represent mean ± SEM. n=3 independent experiments. Significance determined by one-way ANOVA analysis with Sidak's test for multiple comparisons. **e-g,** *PyMT;UBC-Cre^{ERT+/−};Mtdh^{fl/fl}* cells with or without SND1 knockdown, or with (**f**) or without (**e**) 5 days of 0.02 μg/ml 4-OHT pre-treatment were subjected to the tumorsphere assay and then treated with 200 μM of C26-A6 similar to (**c**). The expression of SND1 and MTDH was validated by western blot analysis (**g**). Data represent mean ± SEM. n=3 independent experiments. Significance determined by two tailed Student's *t*-test. Numerical source data for **a-f** and uncropped blots for **g** are provided.
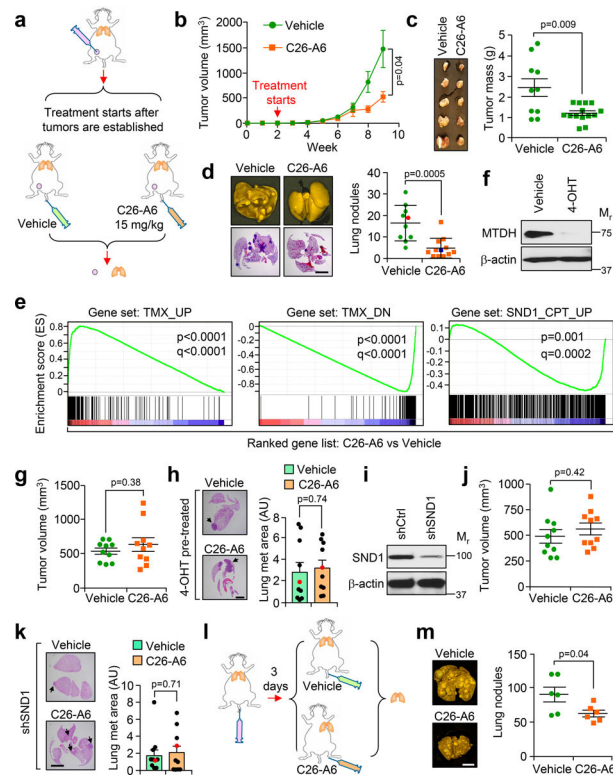
Fig. 6. MTDH-SND1 complex disruption suppresses breast cancer progression and metastasis.
a, Schematic diagram of the treatments in FVB female mice. **b,c,** Tumor size (**b**) and
mass was determined(**c**). Vehicle, n=10 mice, C26-A6, n=12 mice. Size bar, 2 cm. **d,** H&E
staining was performed with lungs, and metastatic nodules were counted. The metastatic
nodules of the representative lungs were highlighted with red and blue respectively. Vehicle,
n=10 lungs; C26-A6, n=12 lungs. Size bar, 5 mm. **e,** Gene set enrichment analysis plot
showing the enrichment of Tmx treatment-upregulated (left), -downregulated (middle), or
SND1-upregulated (right) gene signatures. p and q values were determined by Kolmogorov-
Smirnov statistic with GSEA v3.0. **f-h,** *PyMT;UBC-Cre^{ERT+/−};Mtdh^{fl/fl}* tumor cells with
4-OHT pre-treated were assessed by western blot (**f**). 10k of the cells were inoculated into
FVB female mice and treated with or without C26-A6after primary tumors reached to ~2
mm in diameter. 6 weeks after treatment, tumor size (**g**) and spontaneous lung metastasis (**h**)
was determined. The lung metastatic areas of the representative lungs were highlighted with
red (**h**). Vehicle, n=10 mice; C26-A6, n=10 mice. Size bar, 5 mm. **i-k,** PyMT tumor cells
with endogenous SND1 stably knockdown was confirmed by western blot (**i**). 10k of the
cells were injected into FVB females and treated similarly as in (**g, h**). Tumor size (**j**) and
lung metastasis (**k**) was assessed. The lung metastatic areas of the representative lungs were
highlighted with red (**k**). Vehicle, n=10 mice; C26-A6, n=10 mice. Size bar, 5 mm. **l,m,** 2k
of PyMT tumor cells were injected into FVB femalesvia tail-vein. 3 days after injection, the
mice were treated with vehicle or C26-A6 (**l**). 5 weeks later, lung metastatic nodules were
counted (**m**). n = 6 mice per group. Data represent mean ± SEM. Significance determined by
Two-Way Repeated Measures ANOVA test (**b**) and two tailed Student's *t*-test (**c,d,j,h,k,m**).

AU: arbitrary units. Numerical source data for **b-d, g, h, j, k, m** and uncropped blots for **f** and **i** are provided.
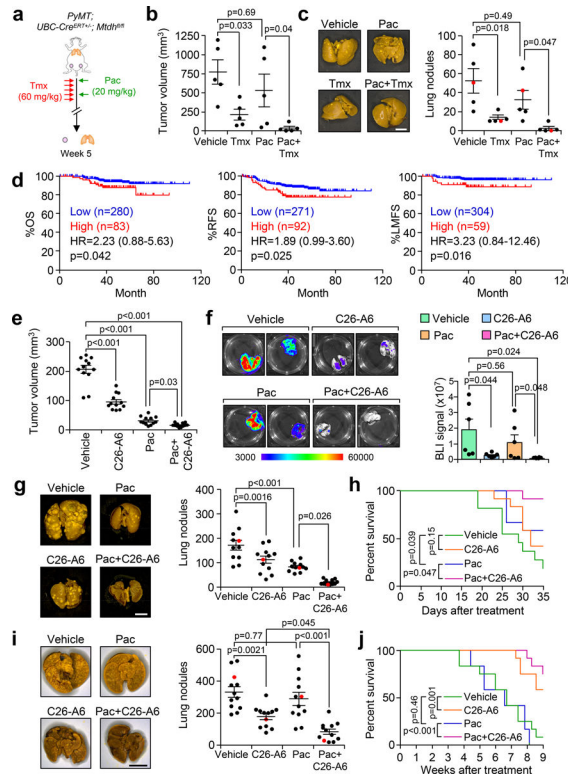
Fig. 7. MTDH-SND1-targeting and chemotherapy synergistically suppress breast cancer progression and metastasis.

a-c, *PyMT;UBC-Cre^{ERT+/−};Mtdh^{fl/fl}* mice treatment scheme (**a**). Primary tumors (**b**), and spontaneous lung metastatic nodules were quantified (**c**). The metastatic nodules of the representative lungs were highlighted with red (**c**). n = 5 mice per group. Size bar, 5 mm. **d,** Kaplan-Meier plots of overall survival (OS), relapse-free survival (RFS), and lung metastasis-free survival (LMFS) of TNBC patients. **e,** NSG female mice were injected with 10k of SCP28 cells. One week after injection the mice were treated with C26-A6 or Paclitaxel (Pac) alone or in combination for 5 weeks. Primary tumor size was measured. n = 6 mice per group. **f,** Lungs from (**e**) were harvested and BLI signal was measured to determine spontaneous lung metastasis. Data represent mean ± SEM. n=6 lungs. **g,** Balb/C females were injected with 1000 4T1 cells via tail-vein. 3 days after injection, the mice were performed similar treatment as in (**e**) for 5 weeks. Lungs were fixed, and the metastatic nodules were counted. The metastatic nodules of the representative lungs were highlighted with red. Vehicle, n=11 mice; n = 12 mice for other groups. Size bar, 5 mm. **h,** Survival rate of the mice in experiment (**g**) was plot. **i,j,** SCP28 primary tumors were removed in NSG female mice when they reached to ~5 mm in diameter. The mice were treated with C26-A6 and Pac alone or in combination. Lungs were collected to count metastatic nodules at endpoint (**i**). The metastatic nodules of the representative lungs were highlighted with red (**i**). Survival rate in each group was analyzed (**j**). n=12 mice per group. Size bar, 5 mm. Data represent mean ± SEM. Significance determined by one-way ANOVA analysis with Sidak's test for multiple comparisons (**b,c,e,f,g,i**) and two-sided Log-rank test (**d,h,j**). Numerical source data for **b-j** are provided.
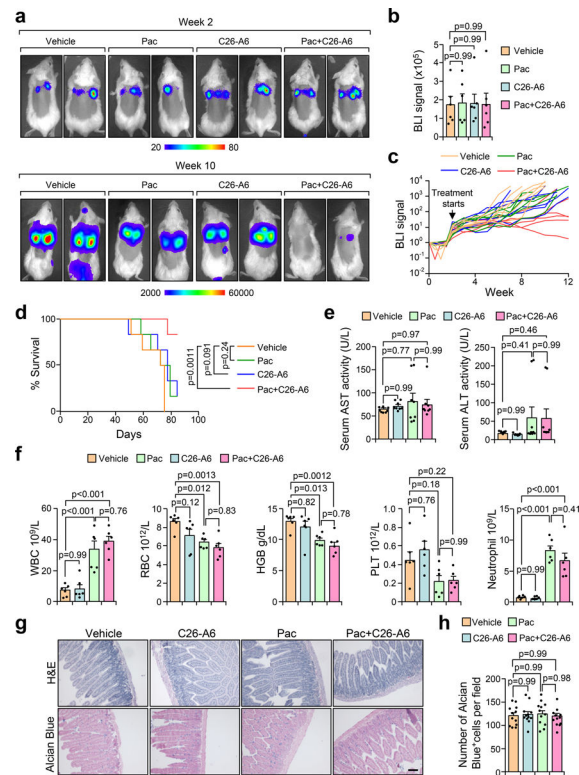
Fig. 8. C26-A6 enhances chemotherapy response in metastatic breast cancer model without additional toxicity.

a-d, 2k 4TO7 cells were injected into Balb/C females. 2 weeks after the injections, the mice were randomized based on lung metastasis that indicated by BLI, and were divided into four groups followed by vehicle, paclitaxel (Pac), and C26-A6 treatment alone or in combination. For Pac, the mice were treated with 20 mg/kg of Pac twice per week for the first two week and then once per week after that, For C26-A6, the mice were treated with 15 mg/kg of C26-A6 5 days per week. Representative mice right before the treatment (week 2) and at week 10 are shown (**a**). The BLI signal was quantified at week 2 (**b**). The metastasis progression of each individuals is shown (**c**). Survival rate in each group was analyzed (**d**). n=6 mice per group. Data represent mean ± SEM. Significance determined by one-way ANOVA analysis with Dunnett's test for multiple comparisons (**b**) or two-sided Log-rank test (**d**). **e,** Serum from mice in (**a**) were collected for ALT and AST activity measurement following the standard protocol (Sigma). Data represent mean ± SEM. AST, n=8 replicates from 6 mice; ALT, n=9 replicates from 6 mice. Significance determined by one-way ANOVA analysis with Sidak's test for multiple comparisons. **f,** Blood samples were drawn from the heart of mice in (**a**), and blood cell counts were performed with the Sysemx XN-3000 Hematology System (Sysmex America, Inc.). Data represent mean ± SEM. n=6 mice per group. Significance determined by one-way ANOVA analysis with Sidak's test for multiple comparisons. **g,** Small intestine samples were obtained from mice in (**a**). H&E and Alcian blue staining was performed on processed, sliced samples. Scale bar: 200 μm. **h,** Quantification of Alcian blue staining results from (**g**). Data represent mean ± SEM. n=12 fields from 6 mice in each group. Significance determined by one-way ANOVA

analysis with Sidak's test for multiple comparisons. Numerical source data for **b-f** and **h** are provided.